Constraining the conditions of phosphogenesis: stable isotope and trace element systematics of Recent Namibian phosphatic sediments

Kaarel Lumiste[1]*, Kaarel Mänd[1,2], Jake Bailey[3], Eva E. Stüeken[4], Kärt Paiste[1,5], Liisa Lang[1], Holar Sepp[1], Aivo Lepland[1,6,7], Kalle Kirsimäe[1]

[1]Department of Geology, University of Tartu, Ravila 14A, 50411 Tartu, Estonia

[2]Department of Earth and Atmospheric Sciences, University of Alberta, Edmonton T6G 2E3, Canada

[3]Department of Earth Sciences, University of Minnesota–Twin Cities, Minneapolis, 55455, USA

[4]School of Earth and Environmental Sciences, University of St. Andrews, KY169 AL, Scotland, United Kingdom

[5]Department of Earth and Planetary Sciences, Washington University in St Louis, St Louis, MO 63130, USA

[6] CAGE – Centre for Arctic Gas Hydrate, Environment and Climate, Department of Geosciences, UiT The Arctic University of Norway, 9037 Tromsø, Norway

[7]Geological Survey of Norway, 7491 Trondheim, Norway

*Corresponding author: email kaarel.lumiste@ut.ee

Abstract

Modern phosphogenesis occurs on continental margins influenced by upwelling and high primary productivity. The formation of phosphatic sediments is coupled to global climate fluctuations, biological cycling of phosphorus and local redox conditions. Although the processes involved in phosphogenesis are well described, high-resolution data on the redox and stable isotope systematics in Recent *in-situ* phosphorites are scarce. In this contribution, we investigate the trace element and sulfur, nitrogen and organic carbon stable isotope composition of Recent *in-situ* phosphatic sediments off the coast of Namibia. Also, we examine the reliability of different widely used geochemical proxies in phosphatic sediments. Our results suggest a shift from sulfidic to suboxic conditions, coinciding with the maximum in solid calcium phosphate mineral concentration. This shift is accompanied by unidirectional changes in Mo and Re enrichments and TOC abundance. Relatively low pyrite $\delta^{34}S$ values (ca -20‰) of phosphatic sediments indicate open system fractionation during phosphogenesis. The initiation of phosphogenesis is also accompanied by negative shifts in

sedimentary $\delta^{13}C_{org}$ and $\delta^{15}N$ values. Phosphate associated sulfate (PAS) $\delta^{34}S$ values are lower than modern seawater sulfate values, suggesting the involvement of chemolithotrophic sulfur oxidation. Our results show a shift in redox conditions from sulfidic to (sub)oxic, coupled with active sulfur cycling are prerequisites for phosphogenesis. Phosphatic sediments show substantial enrichments in U and V highlighting the complexity of using these elements, as well as V/(V+Ni) and V/Cr, as redox proxies particularly in phosphorites and phosphatic sediments.

1. Introduction

Phosphorus is a key limiting macronutrient on geological timescales (Tyrrell, 1999) and understanding the intricacies of the phosphorus cycle is, therefore, crucial for deciphering the interactions between the biosphere, atmosphere-hydrosphere and lithosphere. A key link in the P-cycle is phosphogenesis – the formation of sedimentary phosphates – representing the ultimate sink for marine phosphorus (Ruttenberg and Berner, 1993). Phosphogenesis is a complex phenomenon resulting from an interplay of a variety of physical, biological and chemical factors (Arning et al., 2009a; Brock and Schulz-Vogt, 2011; Föllmi, 1996; Goldhammer et al., 2010; Krajewski, 1994; Mänd et al., 2018; Schulz and Schulz, 2005). The oldest known phosphatic sediments (Lepland et al., 2014; Soares et al., 2019) appear in the Paleoproterozoic, in response to environmental changes triggered by the Great Oxidation Event (Bekker and Holland, 2012; Holland, 2006). The first economically significant episode of phosphorite (i.e. rocks containing at least 9 wt.% of P_2O_5; Filippelli, 2011) formation coincides with the Neoproterozoic Oxygenation Event, possibly related to (bio-)evolutionary advances (Shields et al., 2000) and expansive oxidative weathering (Pufahl and Groat, 2017), which caused enhanced mobilization and cycling of P, which, in turn, led to boosted bioproductivity and eventually to the large-scale burial of phosphatic sediments.

Nearly all of the largest Phanerozoic phosphorites have formed at upwelling continental margins during periods of fluctuating climate and enhanced weathering (Compton et al., 2002; Compton and Bergh, 2016; Föllmi, 1996; Föllmi et al., 2019; Pufahl and Groat, 2017; Schöllhorn et al., 2020; Shields et al., 2000). Similarly, modern phosphogenesis occurs on the continental shelfs of Peru and Chile (Arning et al., 2009b, 2009a; Burnett, 1977), Namibia (Baturin, 2000; Compton et al., 2002; Compton and Bergh, 2016), Baja California (Jahnke et al., 1983), the Arabian Sea (Schenau et al., 2000) and Western Australia (Heggie et al., 1990; O'Brien and Veeh, 1980). With the exception of the lattermost of these sites, the rest of the

major modern sites of phosphogenesis are found on continental margins influenced by strong upwelling of cold nutrient-rich water from the deep ocean (Föllmi, 1996). High primary production, made possible by the upwelled nutrients, leads to the accumulation of large quantities of organic matter. Subsequent degradation of this organic matter liberates organic-bound P and increases pore-water phosphate concentrations, leading to phosphate precipitation, typically in the form of the Ca-phosphate mineral apatite (Arning et al., 2009a).

The formation of apatite is thought to occur during early diagenesis in the topmost few centimeters of the sediment column (Schulz and Schulz, 2005). Initially, amorphous Ca-phosphate precursors precipitate from supersaturated pore-water, which then transform over time to a stable carbonate-rich fluorapatite (Krajewski, 1994). In order to precipitate apatite precursor phases, significant build-up of interstitial phosphate is needed. Increase in pore-water phosphate has been attributed to microbial organic matter degradation (Arning et al., 2009a; Glenn et al., 1994), dissolution of biogenic apatite (Froelich et al., 1988) as well as Fe-Mn oxyhydroxide cycling (Jarvis et al., 1994; Noffke et al., 2012) or “bacterial pumping” (Schulz and Schulz, 2005). A combination of these different processes can raise the pore-water PO_4^{3-} concentrations to levels necessary for the precipitation of Ca-phosphate phases (Arning et al., 2009b; Goldhammer et al., 2010).

Dissolved phosphate buildup in pore-water mediated by Fe-Mn oxyhydroxide cycling (Noffke et al., 2012) and/or by sulfur oxidizing bacteria (Schulz and Schulz, 2005) have been suggested as the most significant pre-concentration processes leading to Ca-phosphate precipitation. Fe-Mn oxyhydroxide transport operates by repeated delivery and release of phosphate adsorbed onto oxide particles under oscillating redox conditions (Pufahl and Grimm, 2003) or through repeated mixing of Fe-Mn phases over the redox boundary by bioturbation (Jarvis et al., 1994), resulting in build-up of the interstitial phosphate concentration. In addition, shallow subsurface sediments at upwelling sites are densely populated (up to 50 g/m^2) by large sulfur bacteria (LSB) such as *Thiomargarita namibiensis* (Schulz et al., 1999) as well as other polyphosphate-metabolizing organisms (Zoss et al., 2018). LSB use nitrate or oxygen as an electron acceptor to oxidize sulfide (Schulz and Schulz, 2005) but can also accumulate phosphate intracellularly as polyphosphate in their vacuoles during (sub)oxic periods and metabolize the compound during periods of sulfidic conditions. Thus, by releasing the hydrolyzed polyphosphate into the surrounding pore-water the interstitial phosphate concentration can be built up to levels required to initiate spontaneous Ca-phosphate precipitation (Brock and Schulz-Vogt, 2011; Schulz and Schulz,

2005). Moreover, LSB microbial mats can play an additional role in phosphogenesis by providing exopolymeric substances acting as substrates for primary nucleation of Ca-phosphate phases (Mänd et al., 2018). Polyphosphate accumulation by LSB takes place only under energetically favorable conditions, when sufficient nitrate or oxygen is available, whereas phosphate is released during sulfidic periods (Brock and Schulz-Vogt, 2011). Similarly, the Fe-Mn oxyhydroxides take up P from oxic seawater and release the particle-bound P during reductive dissolution, which occurs in a suboxic zone below the sediment–water interface (SWI) after the depletion of pore-water oxygen and nitrate (Tribovillard et al., 2006). Because of this dependence on oxygen depletion, both bacterial and Fe-Mn oxyhydroxide "pumping" are redox-dependent processes that take place within sediments near the fluctuating (sub)oxic-anoxic transition zone. Remineralization of abundant organic matter in phosphogenic sites rapidly depletes the supply of electron acceptors, causing the development of shallow and sharp redoxclines near the SWI which, then, act like an "on-off" switch for the precipitation of Ca-phosphate

Another factor controlling Ca-phosphate precipitation is pore-water carbonate alkalinity (Glenn and Arthur, 1988). High rates of microbial sulfate reduction lead to an increase in pore-water HCO_3^- concentrations (Berner et al., 1970), which inhibits apatite precipitation at pH <9 by the formation of ion pairs between dissolved carbonate and Ca^{2+}, resulting in a decrease of free calcium ions by competing Ca-carbonate precipitation (Nathan and Sass, 1981; Glenn and Arthur, 1988; Song et al., 2002). As a result of the relatively narrow pH and Eh ranges that are conducive to the biological and geochemical transformations involved, primary phosphogenesis is limited to shallow sediments directly beneath the SWI.

Earlier studies have highlighted the link between suboxia and modern phosphogenesis (e.g., Arning et al., 2009b; Baturin, 2000; Benmore et al., 1983; Compton and Bergh, 2016; Föllmi, 1996; Glenn et al., 1994; Glenn and Arthur, 1988; Ingall and Jahnke, 1994; Schuffert et al., 1998; Schulz and Schulz, 2005). Numerous studies have used mineralogical, geochemical and isotope proxies to delineate the paleoredox conditions of phosphogenesis through Earth´s history (e.g., Álvaro et al., 2016; Baturin et al., 2014; Berndmeyer et al., 2012; Birski et al., 2019; Bradbury et al., 2015; Daesslé and Carriquiry, 2008; Garnit et al., 2017; Jahnke et al., 1983; Joosu et al., 2016, 2015; Lepland et al., 2014; Schöllhorn et al., 2020; Wallin, 1989). However, the majority of phosphogenesis takes place under dynamic redox and sedimentary settings and phosphatic sediments forming near the seafloor can be prone to reworking and winnowing due to the relatively high specific gravity of sedimentary apatite (2.9 g/cm^3;

Föllmi, 1996). Hence, geochemical data are scarce from *in-situ* phosphatic sediments where phosphate precipitation is or has been recently taking place, as opposed to reworked/winnowed phosphorite deposits where geochemical signatures of the precipitation environment can be muted (e.g., Lumiste et al., 2019). In this study we present high-resolution trace element and stable isotope data from Namibian Shelf sediments containing autochthonous *in-situ* Recent sedimentary apatite. We assess the redox conditions and stable isotope systematics and evaluate the validity of different geochemical and isotope proxies as reflecting the environmental conditions during phosphogenesis.

2. Geological setting

The Namibian Shelf was formed after the breakup of Gondwana. It is characterized as an unusually deep (Compton and Bergh, 2016) and broad (50-150 km; Brüchert et al., 2006; Compton and Bergh, 2016) passive continental margin. The basement of the shelf is made up of Precambrian rocks, overlain by Jurassic to Cenozoic sedimentary rocks, which are truncated by an erosional surface (Compton and Bergh, 2016). The patchy sediment cover of the shelf, while poorly documented, varies from Pleistocene to Recent in age (Compton and Bergh, 2016). The Kunene and Orange rivers are the only perennial rivers that carry sediments to the shelf. Instead, a significant portion of terrigenous sediments is delivered to the shelf by eolian transport (Eckardt and Kuring, 2005).

The Benguela Upwelling System (BUS) is the most productive modern eastern boundary upwelling system (0.37 Gt C/yr; Carr, 2001). It plays a crucial role in determining the (geo)biochemical environment of the shelf. Dominant northwards winds carry surface water away from the shelf, which is compensated by upwelling of nutrient-rich cold deep water (Carr, 2001). This influx of nutrients is utilized by the biosphere, leading to high primary production, and in turn, to high abundance of sinking organic matter. Remineralisation of this organic matter causes a steep suboxic-sulfidic redoxcline in the sediments. These shallow redoxclines fluctuate depending on the intensity of primary production in the overlying water column (Brüchert et al., 2000). Shifts in redox conditions can lead to significant sulfide build-up in the topmost <10 cm of the sediment column (Brüchert et al., 2006) and can, in some cases, even result in eruptions of sulfide or “sulfide blooms” to the water column (Emeis et al., 2004).

Sediments on the shelf, varying from quartz sands to organic-rich diatomaceous mud, contain patchy phosphorite deposits ranging from Miocene to Recent in age (Baturin, 2000; Compton

and Bergh, 2016). The first appearance of sedimentary apatite enrichments on the Namibian Shelf coincides with the initiation of the BUS, following the Late Miocene global cooling phase (Hoetzel et al., 2017). Apatite containing sediments on the shelf can be broadly divided into two distinct groups: reworked phosphorites and phosphatic sediments on the middle and outer shelf and *in-situ* phosphatic sediments on the inner shelf (Baturin, 2000; Compton and Bergh, 2016). The current locus of phosphogenesis on the Namibian inner self is located in the organic rich diatomaceous ooze belt near Walvis Bay (Baturin, 2000; Compton et al., 2002; Compton and Bergh, 2016; Mänd et al., 2018). Deposits on the middle and outer shelf are reworked and winnowed with apatite concentrations reaching 28 wt.% (Mänd et al., 2018). Reworked apatite grains are well rounded, 200-500 µm in size, and contain pyrite and barite inclusions (Lumiste et al., 2019). Phosphatic sediments on the inner shelf contain less apatite (<15%), alongside quartz, plagioclase, K-feldspar, calcite and glauconite (Mänd et al., 2018). The apatite grains in these sediments are subangular to poorly rounded pore fillings, which, along with coexisting fragile diatom frustules, are indicative of *in-situ* origin. The authigenic grains are smaller (<300 µm, Lumiste et al., 2019). Concentric layering of secondary apatite in some grains points towards a complex and episodic phosphogenesis under dynamic redox conditions (Lumiste et al., 2019; Mänd et al., 2018). The age of both types of apatite grains is poorly constrained; the *in-situ* sediments were likely deposited during the Pleistocene to Holocene (Baturin, 2000), whereas the reworked deposits are younger than 5.8 Ma (Compton and Bergh, 2016).

3. Materials and methods

Studied sediment core was collected using an Ocean Instruments MC-400 multi-corer on-board R/V Mirabilis in May 2015. Core 25005 (Fig. 1) was retrieved from phosphatic sediments on the inner shelf (Lat.: 25° S, Long.: 14.74° E, ~ 50 m b.s.l, core length 25 cm) in an area where the density of *Thiomargarita* bacterial mats have been measured to be 50-100 g/m^2 (Brüchert et al., 2006). The sediment core was sampled at 1 cm intervals for the top 10 cm, and 2 cm intervals below that, and the samples were freeze dried.

To study the petrographic characteristics of phosphatic sediments, bulk samples from Core 25005 were mounted on scanning electron microscope stubs and analyzed using optical microscopy and a variable pressure Zeiss EVO MA15 scanning electron microscope (SEM) at University of Tartu.

Bulk sediment trace elemental compositions were measured at Bureau Veritas labs in Vancouver, Canada. A 0.25 g subsample was digested in HNO_3, $HClO_4$ and HF and measured by inductively coupled plasma mass spectrometry (ICP-MS). Analytical data, detection limits and reference materials are given in Supplementary Table 1. Total phosphorus and sulfur concentrations in core 25005 were reported in Mänd et al. (2018).

To assess the degree of enrichment or depletion of trace elements, the enrichment (EN) was calculated by normalizing the trace element values with Al ($EN_{(element\ X)}$ = X (mg kg^{-1}) / Al (%) (see Bennett and Canfield, 2020 for discussion on different normalization approaches). The molar ratio of organic carbon to sedimentary phosphorus (C_{org}/P; Algeo and Ingall, 2007) was calculated as C_{org}/P = (TOC (wt.%) /12)/(P (wt.%) /30.97).

Phosphate-associated sulfate (PAS) was extracted by applying a modified sample preparation method described by Arning et al. (2009) and Canfield et al. (1986). Prior to sulfide and PAS extraction, the samples were pre-treated with 1M NaCl and 1 M ascorbic acid for 24h to remove the easily extractable sulfate (EES). Ascorbic acid was added to inhibit sulfide oxidation. After pre-treatment the samples were centrifuged and filtered. Around 5 ml of 0.5 M $BaCl_2$ solution was added to the filtrate to precipitate the EES as $BaSO_4$. After 24 h, the EES containing solution was centrifuged and the precipitate was dried.

Chromium reduction was used to extract sulfides from the pre-treated sediment samples (Canfield et al., 1986). The samples were transferred to a glass reaction vessel and around 10 ml of ethanol was added. Samples were flushed with N_2 for 15 min, after which 16 ml of 2 M HCl and 16 ml of 1 M $CrCl_2$ was added to the vessel. The samples were heated on a hotplate for 2 hours. The resulting chromium reducible sulfur (CRS) as H_2S-gas was carried by the N_2 into a trapping vessel containing 0.1 M $AgNO_3$, where the sulfur precipitated as Ag_2S. The residual mixture of sediment sample, 2 M HCl and 1 M $CrCl_2$ was centrifuged and filtered. The filtrate was left to react with 0.5 M $BaCl_2$ for 24 h. The precipitate containing PAS was centrifuged and dried. A separate chromium reduction run was performed where only 2 M HCl was allowed to react with the sample for the first 1 h, prior to adding the $CrCl_2$, to separate the acid volatile sulfides (AVS) from CRS. Samples did not contain enough AVS to determine their sulfur isotope composition.

For determining $\delta^{13}C_{org}$, $\delta^{15}N$ and $\delta^{34}S_{bulk}$ values, the samples were treated overnight with 2 M HCl in order to remove carbonate phases. Decarbonated samples were washed three times with DI water prior to measuring. Total organic carbon (TOC), and C_{org} isotope composition

were measured using an isotope-ratio mass spectrometer (IRMS) Delta V Plus + Flash HT+ Conflo IV at University of Tartu. Measurements were calibrated using IAEA-CH-3 and IAEA-CH-6 standards. Total nitrogen (TN), total sulfur (TS), $\delta^{15}N$ and $\delta^{34}S$ were measured using a MAT253 IRMS + EA IsoLink + Conflo IV at the University of St. Andrews. Calibrations were performed with USGS-40, USGS-41 and USGS-62 for nitrogen and with IAEA-S1, IAEA-S2 and NBS-127 for sulfur. Standard errors were less than 0.2‰ for $\delta^{15}N$ and less than 0.5‰ for $\delta^{34}S$. Results are reported as standard delta notations relative to international standards: atmospheric N_2 gas for nitrogen, Vienna PeeDee Belemnite (V-PDB) for carbon and Vienna-Canyon Diablo Troilite (V-CDT) for sulfur.

4. Results

Sediments in Core 25005 change from apatite poor diatomaceous mud in the lower part of the core to apatite-rich sands at the top of the core (Fig. 2.a-b). Fragile complete diatom frustules are abundant throughout the core, especially below 10 cm, where complete and/or fragmented frustules make up a significant portion of the sediment. In addition, intact calcareous ostracod and mollusc shells are present throughout the core. The terrigenous components of the sediment vary from mud to fine sand in size and are composed of quartz, plagioclase, K-feldspar and glauconite. Terrigenous grains are typically angular or rounded to a low degree and can form fragile ~0.5 mm sized aggregates with organic matter (Fig. 2a-b).

Apatite grains are 50-300 µm in size, elongated, subangular to subrounded throughout the core. The surfaces of the grains are irregular and pitted (Fig. 2c-f). Frequently, the grains are covered by thin non-phosphatic clay and/or organic films, giving the grains a mottled appearance under SEM imaging.

4.1. Major and trace elements

Major and trace elemental concentrations in the studied samples are given in Supplementary Table 1. Phosphorus concentrations in sediments increase from 1.1 wt.% at the top of the core to 1.6-1.9 wt.% in the interval from 5 to 9 cm. Further down the values drop to around 1 wt.% at 9-11 cm and below 0.5 wt.% from 11 to 25 cm (Fig. 3). The trend of P-concentrations in the sediment is broadly mirrored by sulfur with low concentrations of ca. 0.6 wt.% within the top 9 cm and an increase to >1 wt.% in the lower part of the core below 11 cm (Fig. 3). Al concentrations are stable throughout the core, with values ranging from 3.1 to 4.2 wt%.

The trace element compositional trends and enrichments reveal two distinct zones (Fig. 4a-d). The upper part of the core (0-10 cm) is characterized by low concentrations of Mo (on average 3.6 mg/kg), Ni (35.2 mg/kg), Cu (15.2 mg/kg), Re (0.023 mg/kg) and Mn (484.5 mg/kg), but elevated concentrations of V (118.5 mg/kg), U (11 mg/kg), Th (13.7 mg/kg), Cr (282.2 mg/kg) and ∑REE (195.8 mg/kg). Sediments in the deeper part of the core below 10 cm contain higher average Mo (8.1 mg/kg), Ni (44.4 mg/kg), Re (0.05 mg/kg) and Cu (28.2 mg/kg) but are lower in V (70 mg/kg), U (5.8 mg/kg), Th (5.6 mg/kg), Cr (159.9 mg/kg), Mn (229.4 mg/kg) and ∑REE (83.4 mg/kg).

EN values vary significantly (Fig. 4). In the upper part, the average Mo_{EN}, V_{EN}, U_{EN}, Re_{EN} values are around 1, 35.2, 3.3 and 6.9, whereas the EN values for the lower part are 2.15, 18.4, 1.5 and 13.2, respectively.

4.2. Stable isotopes

The TN, TS, TOC and stable isotope data are shown in Supplementary Table 2. Sediment $\delta^{13}C_{org}$ values vary from -21.8 ‰ to -19.5‰ with the upper part of the core (0-9 cm) containing ca 1.5‰ lighter biomass than the lower part (Fig. 5a). TOC values are stratigraphically variable, with average values of 1.7 wt.% in the upper part and 3.8 wt.% in the lower part of the core (Fig. 5b). TOC and $\delta^{13}C_{org}$ stratigraphic profiles are similar and values show good correlation with the more negative $\delta^{13}C_{org}$ values corresponding to the lowest TOC values. The $\delta^{15}N$ values vary from 5.3 to 8.1‰, with an average of 6.1‰ (Fig. 5c). The TN values are rather stable from ca. 0.14 wt.‰ in the upper part, to 0.25 wt.‰ in the lower section (Table 2).

CRS $\delta^{34}S$ values increase progressively with depth from -22.1‰ at the sediment surface to 3.3‰ at the bottom of the studied sediment core (Fig. 6a). A rapid transition from negative to positive values occurs at 8-10 cm. Both phosphate associated sulfate (PAS) and easily extractable sulfate (EES) $\delta^{34}S$ values follow similar trends throughout the core and the $\delta^{34}S_{PAS}$ values are as much as 4 ‰ lower than the modern seawater sulfate (21‰; Paytan et al., 1998). The upper part of the core has sulfate $\delta^{34}S$ values of approximately 19‰ and 18‰ for PAS and EES, respectively (Fig. 6b). EES isotope values drop below seawater sulfate values at around 10 cm. PAS remains lighter than seawater sulfate throughout the whole core, showing only 3.7‰ variability between highest and lowest measured values.

5. Discussion

Uptake of redox-sensitive elements (RSE) by authigenic apatite is dependent on and reflective of the environmental conditions in which precipitation occurs. The Namibian Shelf is a dynamic depositional setting (Compton and Bergh, 2016), characterized by erosion and lateral transport of sediments by bottom currents (Inthorn et al., 2006). These sedimentary processes can cause redistribution of apatite and its concentration by winnowing and may complicate the reconstruction of apatite precipitation environments and corresponding elemental budgets. The studied Core 25005 from the highly productive inner shelf at the margin of the Lüderitz upwelling cell (Pichevin et al., 2004) contains abundant diatom frustules with a large portion of the frustules being intact and in pristine conditions, displaying intricate morphological features. Such high abundance of low density, mechanically weak diatom frustules (Miklasz and Denny, 2010) as well as the poorly rounded habit of terrigenous grains indicate that these sediments have escaped extensive reworking and winnowing. The morphology of apatite grains from Core 25005 is in stark contrast to reworked grains on the middle and outer shelf (see Fig. 4 in Mänd et al., 2018). Apatite grains in Core 25005 (Fig. 2c-f) are small, porous and less rounded compared with the pelletal apatite grains from deeper parts of the shelf (Mänd et al., 2018). The internal structure of apatite grains in Core 25005 further point towards their pristine condition, with the absence of pyrite inclusions as well as little or no concentric layering and no secondary apatite growth (Lumiste et al., 2019). The morphology of both the apatite and terrigenous grains coupled with abundant diatom frustules point towards an *in-situ* origin of the phosphatic sediments in Core 25005.

5.1. Redox-sensitive elements

Our results show a direct link between a shift towards less reducing redox conditions and increased accumulation of apatite inferred from redox-sensitive element ratios and isotope data. Some redox-sensitive elements (e.g. Mo, Ni, V, Re and U) behave (quasi-)conservatively under oxic seawater conditions but become enriched in sediments accumulating under reducing conditions (Tribovillard et al., 2006). However, due to the crystal structure of apatite, a wide variety of chemical substitutions can replace Ca, PO_4 and/or F. Many of these substituting elements (i.e. REE, U, V; Pan and Fleet, 2002) are frequently used in redox reconstructions, which can complicate interpretations regarding redox conditions of phosphogenesis.

Algeo and Li (2020) and Bennett and Canfield (2020) have highlighted that Mo, U, Re as well as some other transition metals (e.g., V, Cu, Co, Ni) are the most useful RSE-s for redox analysis with well-differentiated thresholds for distinct redox conditions and depositional environments. In Core 25005, Mo_{EN} and Re_{EN} show similar stratigraphic trends with values of ca. 1 and 7 in the upper phosphatic zone and a two-fold increase to values of ca 2 and 13 in the lower non-phosphatic zone, respectively (Fig. 4a, d). In contrast, vanadium and uranium are enriched in the upper phosphatic zone with V_{EN} and U_{EN} profiles exhibiting a good correspondence with the P profile ($r = +0.94$, p-value <0.01, $n = 18$; $r = +0.97$, p-value <0.01, $n = 18$ for V_{EN}-P and U_{EN}-P, respectively). V_{EN} values vary between 27-40 in the phosphatic zone and decline sharply to ca. 20 in the non-phosphatic zone (Fig. 4b). U_{EN} increases from ca. 2 at the sediment water interface to 4.5 in the lower part of the phosphatic zone and decreases to 1-1.5 in the non-phosphatic zone (Fig. 4c).

Authigenic Mo enrichment is typically controlled by the presence of free sulfide. Under oxic conditions, dissolved Mo occurs as an inactive MoO_4^{2-} ion, whereas particle reactive thiomolybdates ($MoO_xS_{4-x}^{2-}$) are the dominant species under suboxic to sulfidic (euxinic) conditions (Tribovillard et al., 2012). Mo is scavenged and precipitated in sulfide-rich environments with iron sulfides and/or as a Fe-Mo-S phase, (possibly in the form on $FeMoS_2(S_2)$; Helz and Vorlicek, 2019), or on organic particles (Dahl et al., 2017). Similarly, Re is enriched via diffusion and fixation as a solid authigenic phase in anoxic sediments (Crusius et al., 1996; Morford et al., 2005). Overall, low enrichment values of Mo and Re in the phosphatic zone of the sediment column point to suboxic to oxic conditions during the deposition of the upper <10 cm thick sediment layer and anoxic (Re_{EN} values of >10 µg kg^{-1} / %, Mo_{EN} values of 2-3 mg kg^{-1} / %), but not necessarily sulfidic, conditions during the formation of the TOC-rich, non-phosphatic zone of the core (Fig. 4). However, the Re enrichment (reaching 3-5 µg kg^{-1}/%) in the phosphatic zone is by far higher than expected for a deposit formed in a typical oxic environment (Re_{EN} < 1.3 µg kg^{-1} / %; Bennett and Canfield, 2020). On the other hand, Re enrichment seems to be higher in sediments influenced by high productivity (Bennett and Canfield, 2020), which could explain the higher values in sediments on the Namibian Shelf, which are influenced by the most productive modern upwelling system (Carr, 2001). Mo concentrations correlate well with TOC abundances (Fig. 7a; $r = +0.92$, p-value <0.01, $n = 18$) with lower Mo and TOC values in the phosphatic zone, signaling a shift towards less reducing conditions during the deposition of phosphatic sediments (Algeo and Lyons, 2006; Tribovillard et al., 2012). Alternatively, the apparent shift

to suboxic-oxic conditions can be caused by seawater diffusion into an open pore space, further enhanced by vertical mixing of surface sediments by bioturbation, allowing oxidants to penetrate deeper into the sediment. Mollenhauer et al. (2007) have estimated the thickness of disturbed sediment layer on the Namibian Shelf to be around 10 cm, coinciding with the observed change in Mo accumulation in Core 25005. However, intensive bioturbation seems unlikely in the studied area, which is characterized by low annually averaged bottom water dissolved oxygen (<20 µm/L, Brüchert et al., 2006) and transient anoxia.

Concentrations of U and V normalized to Al in Core 25005 show, however, enrichment values trending in opposite direction to Mo and Re ($r = -0.79$, p-value <0.01, $n = 18$; $r = -0.59$, p-value <0.01, $n = 18$ for V_{EN}-Mo_{EN} and U_{EN}-Mo_{EN}, respectively), from U_{EN} values of ~3 to <2 and V_{EN} >30 to <20 mg kg^{-1} / % in the phosphatic and non-phosphatic zone, respectively. Vanadium enrichment in sediments proceeds via a two-step process - under suboxic conditions V^{5+} is reduced to V^{4+} (Wu et al., 2019), but under sulfidic conditions the tetravalent V is further reduced to highly insoluble V^{3+} (Wanty and Goldhaber, 1992). Similarly, authigenic enrichment of U occurs via reduction of soluble U(VI) to the insoluble U(IV) and uptake in reduced sediments (e.g., Barnes and Cochran, 1990). Hence, the markedly enriched U and V values in the upper part of Core 25005 would suggest, instead, anoxic depositional conditions (Algeo and Tribovillard, 2009; Tribovillard et al., 2012; Bennett and Canfield, 2020) during deposition of the uppermost 10 cm of the sedimentary column (Fig. 4b, c). However, Algeo and Li, (2020) and Liu and Algeo, (2020) advise against using universal threshold values for a given redox proxy. Ideally, each proxy should be calibrated for each individual paleodepositional system. In this particular case, the authigenic enrichments of U and V in the phosphatic zone are most likely not due to the changes in redox state of the depositional environment and immobilization-precipitation of the vanadium and uranium as reduced V(III) and U(IV) species but rather caused by the preferential uptake of the U and V in Ca-phosphate. Uranium is a common trace/minor element in apatite, occupying Ca^{2+} sites as U^{4+} in the apatite structure, whereas vanadium incorporation occurs by isomorphous substitution of tetrahedrally coordinated trivalent orthovanadate (VO_4^{3-}) for the PO_4^{3-} group in apatite the structure, forming a solid-solution (Pan and Fleet, 2002). Therefore, the U and V enrichments in the phosphatic zone do not reflect depositional conditions and can lead to erroneous conclusions when using U and V or any related proxies (e.g. V/(V+Ni) and V/Cr ratios; Hatch and Leventhal, 1992; Jones and Manning, 1994) as

tools for paleoenvironmental studies in phosphatic sediments (for a more detailed discussion see Algeo and Liu, 2020).

Recently, Abshire et al. (2020) found that U and TOC are decoupled in sediments on the Namibian Shelf. Their results show higher than expected U concentrations at the suboxic shelf break. The authors propose that the majority of organic matter is transported via nepheloid layers from shallower regions of the shelf without significant contributions from sinking fresh organic matter from the overlying water column, resulting in anomalous U enrichment. However, similar "decoupling" of U and TOC is present between the phosphatic and non-phosphatic portion of Core 25005 (Fig. 7b). Abshire et al. (2020) do not provide phosphorus content or mineralogical data in their study but given the high U concentrations in Namibian sedimentary apatite (Lumiste et al., 2019) and the high degree of correlation between U and P in the bulk sediments ($r = 0.98$, p-value <0.01, $n = 18$ in Core 25005), we suggest a much simpler explanation. The decoupling of U and organic matter is likely caused by enhanced sequestering of U from pore-water into apatite in phosphatic sediments. Our results underline that in addition to organic matter (Algeo and Maynard, 2004), apatite may be a significant sink for U in organic-rich marine sediments where remineralization of phosphorus has resulted in phosphogenesis.

Authigenic Mn enrichments can also be used to decipher redox conditions. However, the redox behavior of Mn is dissimilar to other RSE, as under oxic seawater conditions, manganese forms solid Mn-oxyhydroxides (Tribovillard et al., 2006). Upon reaching the redoxcline, reductive dissolution of Mn-oxyhydroxides particles releases Mn^{2+} into pore-water, where it can either diffuse upwards back into the water column, or precipitate as an authigenic carbonate phase (Pedersen and Price, 1982). Due to high solubility under reducing conditions, anoxic-sulfidic sediments tend to be depleted in Mn (Tribovillard et al., 2006) and Mn/Al values significantly higher or lower than 0.01 are indicative of oxic or anoxic conditions, respectively (Osborne et al., 2017). In Core 25005 Mn/Al ratios drop from 0.01 – 0.02 to around 0.006 at a depth of 9-11 cm (Fig. 8) indicative of transition to more reducing conditions down core. However, similar to V and U, Mn is a common substitute in apatite, replacing Ca in the crystal structure (Pan and Fleet, 2002). In Core 25005, P and Mn show a strong correlation ($R^2 = 0.78$), pointing towards enhanced sequestering of Mn by apatite. Although Mn/Al values are in agreement with Mo and Re enrichments regarding the redox history of the sediments, apatite seems to exert primary control on Mn concentrations in phosphatic sediments. Therefore, apatite abundance can influence Mn concentrations in the

sediment in a similar manner to U and V and using Mn-based redox proxies in phosphatic sediments can also lead to inaccurate conclusions

Likewise, caution is advised for using total organic carbon-to-phosphorus (C_{org}/P) molar ratio for differentiating between oxic and anoxic conditions. Algeo and Ingall (2007) have shown an inverse correlation between C_{org}/P molar ratios and redox potential. Sedimentary C_{org}/P ratios can be used as a robust proxy for paleoredox assessment with thresholds of <50 for oxic, 50-100 for suboxic and >100 for anoxic facies. However, if remineralized P becomes concentrated and precipitated as Ca-phosphate, the molar ratio drops to values far less than 10, as observed in Core 25005 (Fig. 9) indicating, in this case, strongly oxic conditions. This finding itself does not contradict the environmental interpretation based on Mo and Re enrichments discussed above, however, the accumulation of phosphorus is influenced, along with redox conditions, by solid phase phosphate nucleation, precipitation mechanisms and kinetics (Mänd et al., 2018). Hence, C_{org}/P molar ratios can lead to erroneous conclusions regarding the redox conditions of the system when studying phosphatic sediments.

5.2. Sulfur isotope systematics

Maximum phosphorus abundance in Core 25005 is found in a ca. 4-5 cm thick zone just above the boundary below which sulfur and TOC concentrations rapidly increase (Fig. 3). Elevated sulfur and TOC concentrations are accompanied by up to 3.2 wt% of pyrite, whereas the pyrite content in the phosphatic zone is <0.7 wt% (see Fig. 3 in Mänd et al., 2019). Dale et al. (2009) have shown that sulfur cycling in BUS sediments is strongly influenced by effective microbial sulfide oxidation driven by LSB. As a consequence, only a small fraction of the total H_2S produced in sediments is precipitated as pyrite and/or trapped as organic sulfur, with a very low overall sulfur burial efficiency (less than 1%). This implies a strong microbial control on sulfur cycling in phosphogenic sediments that involves both oxidative and reductive sulfur metabolisms. Commonly the sulfide in diagenetic pyrite in marine sediments is derived from either microbial sulfate-driven anaerobic oxidation of methane or organoclastic sulfate reduction (Lin et al., 2016). As microbially mediated reduction of sulfate to sulfide favors ^{32}S, the resulting sulfide obtains negative $\delta^{34}S$ values, leaving the residual SO_4^{2-} enriched in the heavier ^{34}S isotope. This fractionation may be as large as 70‰ between the two sulfur species (Canfield et al., 2010; Sim et al., 2011). Since there is only negligible isotopic fractionation (~1‰) during pyrite precipitation utilizing

446 microbially produced sulfide (Price and Shieh, 1979), sedimentary pyrite $\delta^{34}S$ values reflect
447 the pore-water sulfide isotope ratios during their formation.

448 Porewater sulfide $\delta^{34}S$ values in modern (non-euxinic) marine sediments where a steady-state
449 between sulfate diffusion and its microbial reduction has been achieved typically follow a
450 gradual, nearly linear trend downcore, from negative values of around -45 to -40‰ just below
451 the SWI to near seawater sulfate values of 21‰ at the depth of complete sulfate depletion
452 (e.g., Lin et al., 2016; Peketi et al., 2012; Pellerin et al., 2018). The shift towards more
453 positive $\delta^{34}S$ ratios of pyrite is caused by microbial sulfate reduction rates exceeding the
454 replenishment rates of sulfate from the overlying water column (Jorgensen, 1979) and/or
455 increased efficacy of pyrite precipitation in the presence of highly reactive iron. Either way,
456 pyrite $\delta^{34}S$ values would become progressively enriched in ^{34}S, reaching modern seawater
457 sulfate values at the sulfate methane transition zone (Peketi et al., 2012). The concave, kink-
458 shaped trend of the pyrite $\delta^{34}S$ values from -22‰ at the SWI to 3‰ at the bottom of Core
459 25005 (Fig. 6a) indicates a change from open system conditions in the phosphatic zone to
460 more closed system sulfate reduction conditions in the non-phosphatic zone

461 Residual sulfate in the sediment column should become enriched in the heavier ^{34}S isotope
462 with increasing depth, due to distillation of the sulfate pool by microbial sulfate reduction.
463 However, phosphate-associate sulfate (PAS) $\delta^{34}S$ values in Core 25005 do not show any
464 significant stratigraphic trend (Fig. 6b) with $\delta^{34}S_{PAS}$ values varying between 17 and 21‰,
465 slightly lower than the contemporary seawater sulfate value of 21‰. Sulfate is a common
466 structural substituent in sedimentary apatite, with concentrations as high as 2.7 ± 0.3%
467 (McArthur, 1985). Phosphate associated sulfate has been used to assess the influence of
468 microbial processes on phosphogenesis (Arning et al., 2009a; Benmore et al., 1983;
469 Berndmeyer et al., 2012; Theiling and Coleman, 2019) as well as for reconstructing the
470 marine sulfate $\delta^{34}S$ budget through Earth's history (e.g., Goldberg et al., 2005; Shields et al.,
471 2004).

472 The lighter than seawater values in apatite bound sulfate can be interpreted to be indicative of
473 bacterial sulfide oxidization (Arning et al., 2009a). Our results are in line with Arning et al.
474 (2009a) suggesting that the phosphate-associated sulfate in sedimentary apatite forming in
475 phosphogenetic systems is a mixture of two endmembers: marine sulfate and pore-water
476 sulfate resulting from oxidation of isotopically light sulfide. As far as in the uppermost 4 cm
477 the PAS $\delta^{34}S$ values are ca. 2-4‰ lower than seawater sulfate $\delta^{34}S$ (typically around 1‰ for

the rest of the core), simple mixing between two endmembers, (i.e. seawater sulfate and sedimentary sulfide) suggests that in order to explain the PAS $\delta^{34}S$ values (Fig. 10), a maximum of 8.8% of sulfate taken up by apatite was derived from reoxidized sulfide. Another possible source for the less positive PAS values is contamination by easily extractable sulfate (EES) during the sulfur extraction procedure (Berndmeyer et al., 2012). However, the EES $\delta^{34}S$ values from the same interval are not significantly lower and these two different sulfur species do not show strong correlations ($r = 0.49$, p-value = 0.046, $n = 17$). An important implication of the nearly marine sulfate values of PAS is that primary nucleation and precipitations of the phosphate occurs in the topmost portion of the sediment column in a relatively open system with a good diffusive connection to the overlying water column, before microbial consumption has modified the isotopic composition of the pore-water sulfate pool. Still, lower than seawater PAS $\delta^{34}S$ values can only be explained by contribution from sulfide oxidation, consistent with LSB mediated phosphogenesis.

5.3. Carbon and nitrogen isotopes

The $\delta^{13}C_{org}$ values of Core 25005 (Fig. 5a) show that marine organic matter was the dominant source of organic carbon in the sediment, consistent with the absence of large riverine input, low eolian delivery relative to marine bioproduction and low C_{org}/N ratios measured from the Namibian Shelf (Meisel et al., 2011b, 2011a). The $\delta^{13}C_{org}$ values are rather stable at approximately -19.5 to -20‰ in the lower non-phosphatic zone but decrease to -21 ‰ in the phosphatic zone, with TOC abundances and $\delta^{13}C_{org}$ values showing a clear positive correlation ($r = 0.96$, p-value <0.01, $n = 18$; Fig. 5a, b, 11). Meisel et al. (2011) have noted that in organic rich muds on the Namibian Shelf $\delta^{13}C_{org}$ values usually vary between -18 and -20‰ but can occasionally be lower than -21‰. On one hand, the relatively high $\delta^{13}C_{org}$ values (compared to a global average of ca. -25‰ for marine biomass) can be related to sea surface temperatures reaching higher than 25 °C, regulating CO_2 dissolution in the water column and, thus, driving the $\delta^{13}C_{CO2}$ to higher values; on the other hand, $\delta^{13}C_{org}$ values of the diatomaceous muds on the Namibian Shelf can also become ^{13}C enriched at lower surface ocean temperatures of around 16 °C due to high primary production and high relative consumption (Meisel et al., 2011). In our case, the good correlation between TOC and $\delta^{13}C_{org}$ values points toward high primary production (and higher TOC accumulation) in the lower part of the studied profile and declining productivity towards the SWI. This interpretation

would agree with the observed trends in sediments deposited on the Namibian Shelf during the last 100 years, suggesting rising SW temperatures, lowering ^{13}C values and comparably lower primary production rates (Meisel et al., 2011). In these sediments, the negative $\delta^{13}C_{org}$ shift was accompanied by an increase in $\delta^{15}N$ values, exceeding 8.5‰, suggesting higher denitrification rates (and a nitrate deficit; e.g. Tyrrell and Lucas, 2002).

Interestingly, Meisel et al. (2011) also suggested an opposite trend in sediment profiles across the Namibian Shelf, stratigraphically spanning from the middle Holocene to Recent. Namely, that the negative $\delta^{13}C_{org}$ trends down to values as low as -22‰ between 1250 and 1000 yr BP (before present) mark a period of boosted productivity, suggesting surplus input of isotopically light CO_2, probably derived from high-rates of biomass remineralisation leading to "nutrient trapping" (*sensu* Meisel et al., 2011). In this case, the trend to more negative $\delta^{13}C_{org}$ values is accompanied by a simultaneous change towards slightly more negative $\delta^{15}N$ values that may indicate higher primary production rates. A similar trend of declining $\delta^{13}C_{org}$ and $\delta^{15}N$ values is evident in Core 25005 (Fig. 5a, c) where bulk sediment $\delta^{15}N$ values rise gradually through the core from 5.8‰ at 24-25 cm depth to a maximum of 8.1‰ at 10-11 cm and show a quick drop to values between 5.3 and 6.2‰ in the upper part of the profile.

Variations in sedimentary $\delta^{15}N$ ratios typically reflect changes in the extent of nitrate consumption in the surface water (Altabet and Francois, 1994). As the $\delta^{15}N$ values of average oceanic water is estimated to be around 5‰ (Brandes and Devol, 2002; Sigman et al., 2000), similar $\delta^{15}N$ values of bulk sediments in the upper, phosphatic, part of the core suggest an overall balance between the supply and consumption of nitrate. The sharp increase in $\delta^{15}N$ towards more positive values reaching >8‰ at the lower boundary of the phosphatic zone, which also corresponds to the positive shift in redox-sensitive trace element enrichments, could be interpreted as evidence for the development of anoxic conditions and increased water column denitrification rates.

Indeed, water column redox conditions are highly dynamic on the Namibian Shelf and iron limitation and rapid oxidation of organic carbon promotes episodic water column euxinia (Brüchert et al., 2006, 2003; Dale et al., 2009). Under water column anoxia, nitrate is used as an electron acceptor instead of free O_2 for microbial metabolism, leading to ^{15}N enriched nitrate pool (Holmes et al., 1996), and it has been shown that on the Namibian Shelf, episodic sulfidic conditions cause ^{15}N enrichment in the sedimentary $\delta^{15}N$ signature (e.g. Brüchert et al., 2006; Lavik et al., 2009). The positive shift in bulk sediment $\delta^{15}N$ values in the middle of

Core 25005 profile may, therefore, denote the establishment of transient water column euxinia.

The heaviest $\delta^{15}N$ values occur in the same interval where sedimentary phosphate levels start to increase, indicating a temporal relationship between the establishment of the anoxic water column conditions and the onset of phosphogenesis. The Namibian Shelf sediments are a host to abundant LSB (*Thiomargarita* and other large polyphosphate-metabolizing microorganisms; Schulz et al., 1999; Zoss et al., 2018). LSB mainly inhabit suboxic parts of the sediment column, near the SWI, where they oxidize reduced sulfur species to gain metabolic energy. Under oxic conditions LSB are capable of storing nitrate and phosphorus intracellularly, which are then hydrolyzed for energy under anoxic conditions (Schulz and Schulz, 2005). This peculiar metabolic pathway allows sulfur-oxidizing bacteria to survive episodic fluctuations towards more reducing redox conditions (Brock and Schulz-Vogt, 2011). Due to this mechanism, LSB can act as "phosphate pumps", building up the dissolved phosphate level to intermittent supersaturation in pore-water with respect to Ca-phosphate, leading to stable apatite precipitation (Arning et al., 2009b; Goldhammer et al., 2011; Schulz and Schulz, 2005).

The shift in sedimentary $\delta^{13}C_{org}$ values from <-20‰ in the non-phosphatic zone to around -21‰ in the upper part of the core could also be interpreted as a result of the bacterial pump. Although the effects of LSB on the carbon isotope cycle is scarcely documented, Zhang et al., (2005) reported $\delta^{13}C_{org}$ values of approximately -29 ‰ for the biomass of sulfur-oxidizing *Beggiatoa.* The 1.5‰ lighter $\delta^{13}C_{org}$ values in the phosphatic portion of the core could, therefore, be the result of an increased input of isotopically lighter LSB biomass.

5.4. **Implications for phosphogenesis**

Our data show that phosphate accumulation in sediments on the Namibian Shelf is tightly related to redox conditions of the sediments as inferred from the distribution of redox sensitive Mo and Re and stable isotope signatures. Similar relationships with a transition from sulfidic organic-rich sediments to overlying suboxic apatite rich sediments reported in this study have been described in other Cenozoic phosphorites at upwelling margins near Peru (Arning et al., 2009b), Baja California (Föllmi et al., 2019) and Monterey (Föllmi et al., 2005; John et al., 2002) as well as in geologically older deposits (Glenn and Arthur, 1988), suggesting an analogous environmental setting and formation mechanism. The prevalent interpretation regarding the formation of the phosphatic component of these sediments is

574 believed to progress by (a) formation of phosphatic pore fillings during early diagenesis near
575 the SWI (sediment depth of <5 cm; Schulz and Schulz, 2005), (b) formation of phosphatic
576 laminae by repeated episodes of non-deposition that (c) act as a sedimentary "seal", aiding
577 the preservation of organic matter below, (d) leading to sulfidic conditions in the sediment
578 (Arning et al., 2009b; Föllmi et al., 2005; John et al., 2002). However, different from the
579 model above, the apatite grains in Core 25005 do not form uniform laminae that could
580 significantly inhibit the exchange between bottom waters and pore-water. Also, the nearly
581 marine PAS $\delta^{34}S$ and negative pyrite $\delta^{34}S$ values imply that pore-water was not cut off from
582 the overlying water column during the formation of apatite. We suggest that, rather than
583 apatite acting as a seal and causing sulfidic conditions in the pore system, redox fluctuations
584 in the water column from sulfidic to suboxic, brought on by changes in the upwelling and
585 delivery rates of organic matter are controlling the precipitation of apatite. Further, it is
586 peculiar that the ^{15}N-enriched peak in bulk sediment nitrogen isotope values, interpreted as
587 reflecting the establishment of episodic sulfidic water column conditions and pulses of LSB-
588 stored phosphate release, does not correspond with the peak in phosphorus abundance, but
589 rather marks the initiation of phosphate precipitation. Thus, the episodic sulfidic conditions
590 may serve as drivers of phosphate accumulation in pore-waters, but the precipitation of solid
591 phosphate phases is a more complex process.

592 This complexity may be the result of different, but overlapping processes driving phosphate
593 precipitation. Besides the bacterial P-pump, concentration of P via organic matter degradation
594 and the Fe-Mn oxyhydroxide "redox pump" were and still are considered as the most
595 important processes capable of modifying interstitial phosphate concentrations through the
596 release of particle-bound phosphate (Jarvis et al., 1994; Küster-Heins et al., 2010; Noffke et
597 al., 2012; Pufahl and Grimm, 2003). Reductive dissolution of Fe-Mn oxyhydroxides occurs
598 under suboxic conditions (Tribovillard et al., 2006), similar to the bacterial P-pump.
599 Fluctuating redoxclines would increase the effectiveness of this mechanism through
600 accumulation of Fe-Mn oxyhydroxide during oxygenated periods near the SWI and rapid
601 dissolution when the anoxic redoxcline is shifted upwards. Dissolved pore-water Fe^{2+}
602 concentration peaks have been described at similar sediment depth to peak LSB
603 concentrations in the Namibian shelf sediments (2-4 cm, Küster-Heins et al., 2010). Both
604 processes occur in relatively similar conditions near the SWI, making it difficult to
605 distinguish the relative roles of these two mechanisms for interstitial phosphate
606 concentrations. However, seawater-like REE+Y patterns of the apatite grains (Lumiste et al.,

2019) are dissimilar to REE+Y patterns of pore-water influenced by dissolved Fe-Mn oxyhydroxides (e.g. Deng et al., 2017; Haley et al., 2004). This mismatch does not necessarily disprove the involvement of Fe-Mn oxyhydroxide in phosphogenesis but indicates that primary nucleation likely occurs before the dissolution of Fe-Mn particles. Moreover, water column redox conditions are highly dynamic on the Namibian Shelf (e.g. Brüchert et al., 2006), resulting in an inhibited Fe-Mn oxyhydroxide cycle during periods of poorly oxygenated water conditions. Borchers et al. (2005) found that the sediments of the diatomaceous ooze belt – the main locus of modern phosphogenesis – are strongly depleted in Mn and somewhat depleted in Fe, indicating a relatively insignificant role of the Fe-Mn particle shuttle in the sediments.

Pore-water phosphate in modern shelf sediments influenced by upwelling can reach concentrations as high as 300 µM (e.g. Holmkvist et al., 2010; Jahnke et al., 1983; Schulz and Schulz, 2005), several orders of a magnitude higher than in average oceanic seawater (Conkright et al., 2000). Nevertheless, Holmkvist et al. (2010) has shown that pore-water which is supersaturated with respect to apatite in the presence of the high LSB activity does not necessitate the precipitation of apatite, and even if both prerequisites (i.e. supersaturation and presence of the suitable nucleation templates) for phosphogenesis are fulfilled, the precipitation may not occur, and phosphate can diffuse to the overlying water column. It is evident that in addition to pore-water supersaturation with respect to apatite, for precipitation to occur, the nucleation energy barrier must be surpassed. Sedimentary apatite is thought to precipitate via transformation from fluoride-poor metastable amorphous precursor phases (Gunnars et al., 2004; Krajewski, 1994). This type of precipitation is relatively fast-paced, resulting in a short supersaturation-nucleation-depletion cycle in the topmost cm of the sediment column (Krajewski, 1994). These precursor phases (Cappellen and Berner, 1991; Gunnars et al., 2004; Krajewski, 1994) – as well as microbial organic matrix (Mänd et al., 2018) – can act as a nucleation template for apatite precipitation. Moreover, experimental studies have shown that apatite precursors can nucleate homogeneously (Ross et al., 2017); in addition to the utilization of highly variable nucleation surfaces (Krajewski, 1994), as well as high density of growth sites in modern sedimentary apatites (Mänd et al., 2018), these findings indicate that phosphogenesis is not strongly dependant on specific nucleation conditions. On the other hand, close association between organic polymeric macromolecules and apatite in Namibian phosphatic sediments point towards organic matter controlling the primary nucleation (Mänd et al., 2018).

Rather than any particular water column or sediment redox state, phosphogenesis may instead be tied to redox variability. Modern sedimentary phosphorites are found in the periphery of organic-rich muds (Burnett et al., 1983), overlain by oxygen-depleted water masses (Brock and Schulz-Vogt, 2011). A distinct feature of upwelling zones, especially in the case of the margins of organic-rich muds, is spatially heterogeneous redox conditions or "poikiloxia" (Algeo and Rowe, 2012). Redox conditions at the SWI on the shelf are variable both on long (>100 yr; Algeo and Li, 2020; Hoetzel et al., 2017) and short timescales (monthly/daily; Bailey and Chapman, 1991; Brüchert et al., 2003, 2006). These short fluctuations in redox conditions at the SWI can facilitate bacterial P-pumping (*sensu* Brock and Schulz-Vogt, 2011). During low-oxygen bottom water conditions, the redoxcline is shifted above or near the SWI, initiating polyphosphate hydrolysis in LSB and causing phosphate saturation of the pore-water with respect to amorphous precursor phases, which are then rapidly precipitated and subsequently converted to more stable apatite (Jahnke, 1984). The co-occurrence of diagenetic pyrite in phosphate-rich sediments provides evidence for temporary reducing conditions (Fig. 3; Mänd et al., 2018), whereas redox proxies indicate dominantly suboxic conditions during the formation of apatite (Fig. 4a-d).

Additionally, redox fluctuations affect the interstitial alkalinity through organic matter degradation (Glenn and Arthur, 1988). There is a continuous increase in alkalinity in shallow sediments influenced by upwelling (Noffke et al., 2012). A high flux of organic carbon from the water column leads to higher rates of sulfate reduction, which in turn, leads to increased alkalinity (Berner et al., 1970). Apatite precipitation, however, is inhibited in the presence of high alkalinity (Briggs and Wilby, 1996; Föllmi, 1996; Glenn and Arthur, 1988). This suggests that a combination of suitable biohabitats for polyphosphate-metabolizing bacteria with fluctuating water column redox (Brock and Schulz-Vogt, 2011; Schulz et al., 1999) and suitable alkalinity levels (Glenn and Arthur, 1988) limit phosphogenesis to the upper few cm of the sediment. The patchy spatial distribution of phosphorites (e.g. Baturin, 2000; Compton and Bergh, 2016; Mänd et al., 2018) is likely the result of these same factors. On the other hand, sulfide oxidation results in less alkaline conditions. Sulfide diffusing upwards from below the redoxcline and its subsequent oxidation at the suboxic-oxic transition would lead to lower pH near the SWI, inhibiting the formation of carbonates but promoting the precipitation of phosphate (Föllmi, 1996; Theiling and Coleman, 2019).

Conclusions

Our study presents high-resolution redox and stable isotope data from a 25 cm long core containing Recent Namibian *in-situ* phosphatic sediments. The lower part of the core is made up of organic and pyrite-rich non-phosphatic sediments, whereas the upper part is low in TOC and pyrite but contains a significant amount of apatite (up to 1.9 wt.% of P). The transition to phosphatic sediments coincides with changes in redox conditions and sulfur stable isotope systematics. The non-phosphatic portion of the core is enriched in Mo, Re and TOC. These sediments were likely deposited under sulfidic conditions during episodes of extensive upwelling and high organic matter flux. Phosphatic sediments show low levels of Mo and Re enrichment, but authigenic enrichment in V and U that is likely caused by enhanced sequestering of these elements by apatite. Therefore, the use of V and U enrichment, as well as other related proxies (e.g., V/(V+Ni) and V/Cr ratios) in apatite-rich sediments can lead to erroneous conclusions regarding redox conditions.

Changes in redox conditions parallel CRS $\delta^{34}S$ values showing a kink-shaped trend of pyrite $\delta^{34}S$ values, from ^{34}S depleted values at the SWI to slightly positive $\delta^{34}S$ values at the bottom of the core. This trend suggests a change from relatively closed system sulfate reduction conditions in the lower part of the core to a more open system conditions in the upper part. Phosphate associated sulfate (PAS) $\delta^{34}S$ values are consistently lower than seawater sulfate, and a mixing model suggest that up to 8.8% of apatite-bound sulfate is derived from reoxidized sulfide, implying the involvement of LSB in phosphogenesis.

The variation in organic carbon $\delta^{13}C$ and bulk sediment $\delta^{15}N$ values suggest changing primary production rates, establishment of sulfidic conditions and increased water column denitrification rates during the initiation of the phosphogenesis, which is in line with the shift in Re and Mo enrichments. This association implies that the initiation of the bacterial P-pump coincided with the maximum degree of anoxia. As redox conditions became less reducing, phosphate precipitated as a result of the bacterial P-pump, which relies on the availability of nitrate (or oxygen) from the overlying water column and a large sulfide pool in the organic rich sediments directly below.

Acknowledgements

This study was supported by the Estonian Science Agency project PRG447 and the Estonian Centre of Analytical Chemistry. K. Paiste was supported by the European Union's Horizon 2020 research and innovation program under the Marie Skłodowska-Curie grant agreement No 894831. We would also like to thank the organizers and participants of the Regional Graduate Network in Oceanography Discovery Camp 2015, funded by the Agouron Institute and the Scientific Committee for Oceanographic Research (SCOR), as well as the Namibian Ministry of Fisheries and Marine Resources and the captain and crew of R/V Mirabilis for access to the coring site.

References

Abshire, M.L., Romaniello, S.J., Kuzminov, A.M., Cofrancesco, J., Severmann, S., Riedinger, N., 2020. Uranium isotopes as a proxy for primary depositional redox conditions in organic-rich marine systems. Earth Planet. Sci. Lett. 529, 115878. https://doi.org/10.1016/j.epsl.2019.115878

Algeo, T.J., Ingall, E., 2007. Sedimentary Corg:P ratios, paleocean ventilation, and Phanerozoic atmospheric pO2. Palaeogeogr. Palaeoclimatol. Palaeoecol. 256, 130–155. https://doi.org/10.1016/j.palaeo.2007.02.029

Algeo, T.J., Li, C., 2020. Redox classification and calibration of redox thresholds in sedimentary systems. Geochim. Cosmochim. Acta. https://doi.org/10.1016/j.gca.2020.01.055

Algeo, T.J., Liu, J., 2020. A re-assessment of elemental proxies for paleoredox analysis. Chem. Geol. 119549. https://doi.org/10.1016/j.chemgeo.2020.119549

Algeo, T.J., Lyons, T.W., 2006. Mo-total organic carbon covariation in modern anoxic marine environments: Implications for analysis of paleoredox and paleohydrographic conditions. Paleoceanography 21. https://doi.org/10.1029/2004PA001112

Algeo, T.J., Maynard, J.B., 2004. Trace-element behavior and redox facies in core shales of Upper Pennsylvanian Kansas-type cyclothems. Chem. Geol. 206, 289–318. https://doi.org/10.1016/j.chemgeo.2003.12.009

Algeo, T.J., Rowe, H., 2012. Paleoceanographic applications of trace-metal concentration data. Chem. Geol. 324–325, 6–18. https://doi.org/10.1016/j.chemgeo.2011.09.002

Algeo, T.J., Tribovillard, N., 2009. Environmental analysis of paleoceanographic systems

based on molybdenum – uranium covariation. Chem. Geol. 268, 211–225. https://doi.org/10.1016/j.chemgeo.2009.09.001

Altabet, M.A., Francois, R., 1994. Nitrogen isotopic ratio as a recorder for surface. Global Biogeochem. Cycles 8, 103–116.

Álvaro, J.J., Shields-Zhou, G.A., Ahlberg, P., Jensen, S., Palacios, T., 2016. Ediacaran–Cambrian phosphorites from the western margins of Gondwana and Baltica. Sedimentology 63, 350–377. https://doi.org/10.1111/sed.12217

Arning, E.T., Birgel, D., Brunner, B., Peckmann, J., 2009a. Bacterial formation of phosphatic laminites off Peru. Geobiology 7, 295–307. https://doi.org/10.1111/j.1472-4669.2009.00197.x

Arning, E.T., Lückge, A., Breuer, C., Gussone, N., Birgel, D., Peckmann, J., 2009b. Genesis of phosphorite crusts off Peru. Mar. Geol. 262, 68–81. https://doi.org/10.1016/j.margeo.2009.03.006

Bailey, G.W., Chapman, P., 1991. Short-term variability during an anchor station study in the southern Benguela upwelling system: Chemical and physical oceanography. Prog. Oceanogr. 28, 9–37. https://doi.org/10.1016/0079-6611(91)90019-I

Barnes, C.E., Cochran, J.K., 1990. Uranium removal in oceanic sediments and the oceanic U balance. Earth Planet. Sci. Lett. 97, 94–101. https://doi.org/10.1016/0012-821X(90)90101-3

Baturin, G.N., 2000. Formation and Evolution of Phosphorite Grains and Nodules on the Namibian Shelf, from Recent to Pleistocene, in: Glenn, C.R., Prévôt-Lucas, L., Lucas, J. (Eds.), Marine Authigenesis: From Global to Microbial. SEPM Society for Sedimentary Geology.

Baturin, G.N., Zhegallo, E.A., Shkolnik, E.L., 2014. The geochemical similarity of Oligocene and recent phosphorites from the Chiatura deposit (Georgia) and the Namibian shelf. Dokl. Earth Sci. 459, 1533–1538. https://doi.org/10.1134/S1028334X14120022

Bekker, A., Holland, H.D., 2012. Oxygen overshoot and recovery during the early Paleoproterozoic. Earth Planet. Sci. Lett. 317–318, 295–304. https://doi.org/10.1016/j.epsl.2011.12.012

761 Benmore, R.A., Coleman, M.L., McArthur, J.M., 1983. Origin of sedimentary francolite from
762 its sulphur and carbon isotope composition. Nature 302, 516–518.
763 https://doi.org/10.1038/302516a0

764 Bennett, W.W., Canfield, D.E., 2020. Redox-sensitive trace metals as paleoredox proxies: A
765 review and analysis of data from modern sediments. Earth-Science Rev. 204, 103175.
766 https://doi.org/10.1016/j.earscirev.2020.103175

767 Berndmeyer, C., Birgel, D., Brunner, B., Wehrmann, L.M., Jöns, N., Bach, W., Arning, E.T.,
768 Föllmi, K.B., Peckmann, J., 2012. The influence of bacterial activity on phosphorite
769 formation in the Miocene Monterey Formation, California. Palaeogeogr. Palaeoclimatol.
770 Palaeoecol. 317–318, 171–181. https://doi.org/10.1016/j.palaeo.2012.01.004

771 Berner, R.A., Scott, M.R., Thomlinson, C., 1970. Carbonate alkalinity in the pore waters of
772 anoxic marine sediments. Limnol. Oceanogr. 15, 544–549.
773 https://doi.org/10.4319/lo.1970.15.4.0544

774 Birski, Ł., Słaby, E., Wirth, R., Koch-Müller, M., Simon, K., Wudarska, A., Götze, J.,
775 Lepland, A., Hofmann, A., Kuras, A., 2019. Archaean phosphates: a case study of
776 transformation processes in apatite from the Barberton greenstone belt. Contrib. to
777 Mineral. Petrol. 174, 1–23. https://doi.org/10.1007/s00410-019-1560-z

778 Borchers, S.L., Schnetger, B., Böning, P., Brumsack, H.J., 2005. Geochemical signatures of
779 the Namibian diatom belt: Perennial upwelling and intermittent anoxia. Geochemistry,
780 Geophys. Geosystems 6. https://doi.org/10.1029/2004GC000886

781 Bradbury, H.J., Vandeginste, V., John, C.M., 2015. Diagenesis of phosphatic hardgrounds in
782 the Monterey Formation: A perspective from bulk and clumped isotope geochemistry.
783 Bull. Geol. Soc. Am. 127, 1453–1463. https://doi.org/10.1130/B31160.1

784 Brandes, J.A., Devol, A.H., 2002. A global marine-fixed nitrogen isotopic budget:
785 Implications for Holocene nitrogen cycling. Global Biogeochem. Cycles 16, 67-1-67–
786 14. https://doi.org/10.1029/2001gb001856

787 Briggs, D.E.G., Wilby, P.R., 1996. The role of the calcium carbonate-calcium phosphate
788 switch in the mineralization of soft-bodied fossils. J. Geol. Soc. London. 153, 665–668.
789 https://doi.org/10.1144/gsjgs.153.5.0665

790 Brock, J., Schulz-Vogt, H.N., 2011. Sulfide induces phosphate release from polyphosphate in

cultures of a marine Beggiatoa strain. ISME J. 5, 497–506. https://doi.org/10.1038/ismej.2010.135

Brüchert, V., Currie, B., Peard, K.R., Lass, U., Endler, R., Dübecke, A., Julies, E., Leipe, T., Zitzmann, S., 2006. Biogeochemical and physical control on shelf anoxia and water column hydrogen sulphide in the Benguela coastal upwelling system off Namibia., in: Neretin, L.N. (Ed.), Past and Present Water Column Anoxia. Kluwer Academic Publishers, Dordrecht, pp. 161–193. https://doi.org/10.1007/1-4020-4297-3_07

Brüchert, V., Jørgensen, B.B., Neumann, K., Riechmann, D., Schlösser, M., Schulz, H., 2003. Regulation of bacterial sulfate reduction and hydrogen sulfide fluxes in the central Namibian coastal upwelling zone. Geochim. Cosmochim. Acta 67, 4505–4518. https://doi.org/10.1016/S0016-7037(03)00275-8

Brüchert, V., Pérez, M.E., Lange, C.B., 2000. Coupled primary production, benthic foraminiferal assemblage, and sulfur diagenesis in organic-rich sediments of the Benguela upwelling system. Mar. Geol. 163, 27–40. https://doi.org/10.1016/S0025-3227(99)00099-7

Burnett, W.C., 1977. Geochemistry and origin of phosphorite deposits from off Peru and Chile. Bull. Geol. Soc. Am. 88, 813–823. https://doi.org/10.1130/0016-7606(1977)88<813:GAOOPD>2.0.CO;2

Burnett, W.C., Roe, K.K., Piper, D.Z., 1983. Upwelling and Phosphorite Formation in the Ocean, in: Suess, E., Thiede, J. (Eds.), Coastal Upwelling Its Sediment Record: Part A: Responses of the Sedimentary Regime to Present Coastal Upwelling. Springer US, Boston, MA, pp. 377–397. https://doi.org/10.1007/978-1-4615-6651-9_18

Canfield, D.E., Farquhar, J., Zerkle, A.L., 2010. High isotope fractionations during sulfate reduction in a low-sulfate euxinic ocean analog. Geology 38, 415–418. https://doi.org/10.1130/G30723.1

Canfield, D.E., Raiswell, R., Westrich, J.T., Reaves, C.M., Berner, R.A., 1986. The use of chromium reduction in the analysis of reduced inorganic sulfur in sediments and shales. Chem. Geol. 54, 149–155. https://doi.org/10.1016/0009-2541(86)90078-1

Cappellen, P. Van, Berner, R.A., 1991. Fluorapatite crystal growth from modified seawater solutions. Geochim. Cosmochim. Acta 55, 1219–1234. https://doi.org/10.1016/0016-

7037(91)90302-L

Carr, M.E., 2001. Estimation of potential productivity in Eastern Boundary Currents using remote sensing. Deep. Res. Part II Top. Stud. Oceanogr. 49, 59–80. https://doi.org/10.1016/S0967-0645(01)00094-7

Compton, J.S., Bergh, E.W., 2016. Phosphorite deposits on the Namibian shelf. Mar. Geol. 380, 290–314. https://doi.org/10.1016/j.margeo.2016.04.006

Compton, J.S., Mulabisana, J., McMillan, I.K., 2002. Origin and age of phosphorite from the Last Glacial Maximum to Holocene transgressive succession off the Orange ... Origin and age of phosphorite from the Last Glacial Maximum to Holocene transgressive succession o ¡ the Orange River , South Africa. Mar. Geol. 186, 243–261. https://doi.org/10.1016/S0025-3227(02)00211-6

Conkright, M.., Gregg, W.., Levitus, S., 2000. Seasonal cycle of phosphate in the open ocean. Deep Sea Res. Part I Oceanogr. Res. Pap. 47, 159–175. https://doi.org/10.1016/S0967-0637(99)00042-4

Crusius, J., Calvert, S., Pedersen, T., Sage, D., 1996. Rhenium and molybdenum enrichments in sediments as indicators of oxic, suboxic and sulfidic conditions of deposition. Earth Planet. Sci. Lett. 145, 65–78. https://doi.org/10.1016/s0012-821x(96)00204-x

Daesslé, L.W., Carriquiry, J.D., 2008. Rare earth and metal geochemistry of land and submarine phosphorites in the Baja California Peninsula, Mexico. Mar. Georesources Geotechnol. 26, 340–349. https://doi.org/10.1080/10641190802382633

Dahl, T.W., Chappaz, A., Hoek, J., McKenzie, C.J., Svane, S., Canfield, D.E., 2017. Evidence of molybdenum association with particulate organic matter under sulfidic conditions. Geobiology 15, 311–323. https://doi.org/10.1111/gbi.12220

Dale, A.W., Brüchert, V., Alperin, M., Regnier, P., 2009. An integrated sulfur isotope model for Namibian shelf sediments. Geochim. Cosmochim. Acta 73, 1924–1944. https://doi.org/10.1016/j.gca.2008.12.015

Deng, Y., Ren, J., Guo, Q., Cao, J., Wang, H., Liu, C., 2017. Rare earth element geochemistry characteristics of seawater and porewater from deep sea in western Pacific. Sci. Rep. 7, 1–13. https://doi.org/10.1038/s41598-017-16379-1

Eckardt, F.D., Kuring, N., 2005. SeaWiFS identifies dust sources in the Namib Desert. Int. J. Remote Sens. 26, 4159–4167. https://doi.org/10.1080/01431160500113112

Emeis, K.C., Brüchert, V., Currie, B., Endler, R., Ferdelman, T., Kiessling, A., Leipe, T., Noli-Peard, K., Struck, U., Vogt, T., 2004. Shallow gas in shelf sediments of the Namibian coastal upwelling ecosystem. Cont. Shelf Res. 24, 627–642. https://doi.org/10.1016/j.csr.2004.01.007

Filippelli, G.M., 2011. Phosphate rock formation and marine phosphorus geochemistry: The deep time perspective. Chemosphere 84, 759–766. https://doi.org/10.1016/j.chemosphere.2011.02.019

Föllmi, K.B., 1996. The phosphorus cycle , phosphogenesis phosphate-rich deposits 40, 55–124. https://doi.org/10.1016/0012-8252(95)00049-6

Föllmi, K.B., Badertscher, C., de Kaenel, E., Stille, P., John, C.M., Adatte, T., Steinmann, P., 2005. Phosphogenesis and organic-carbon preservation in the Miocene Monterey Formation at Naples Beach, California - The Monterey hypothesis revisited. Bull. Geol. Soc. Am. 117, 589–619. https://doi.org/10.1130/B25524.1

Föllmi, K.B., Schöllhorn, I., Ulianov, A., Adatte, T., Spangenberg, J.E., de Kaenel, E., Gertsch, B., Schwennicke, T., Ledesma, M.C., Grimm, K.A., Garrison, R.E., 2019. Phosphogenesis during the Cenozoic transition from greenhouse to icehouse conditions: Upper Oligocene to lower Miocene siliceous, phosphate, and organic-rich sediments near La Purísima, Baja California Sur, Mexico. Depos. Rec. 5, 23–52. https://doi.org/10.1002/dep2.52

Froelich, P.N., Arthur, M.A., Burnett, W.C., Deakin, M., Hensley, V., Jahnke, R., Kaul, L., Kim, K.H., Roe, K., Soutar, A., Vathakanon, C., 1988. Early diagenesis of organic matter in Peru continental margin sediments: Phosphorite precipitation. Mar. Geol. 80, 309–343. https://doi.org/10.1016/0025-3227(88)90095-3

Garnit, H., Bouhlel, S., Jarvis, I., 2017. Geochemistry and depositional environments of Paleocene–Eocene phosphorites: Metlaoui Group, Tunisia. J. African Earth Sci. 134, 704–736. https://doi.org/10.1016/j.jafrearsci.2017.07.021

Glenn, C.R., Arthur, M.A., 1988. Petrology and major element geochemistry of Peru margin phosphorites and associated diagenetic minerals: Authigenesis in modern organic-rich

880 sediments. Mar. Geol. 80, 231–267. https://doi.org/10.1016/0025-3227(88)90092-8

881 Glenn, C.R., Föllmi, K.B., Riggs, S.R., Baturin, G.N., Grimm, K.A., Trappe, J., Abed, A.M.,
882 Galli-Olivier, C., Garrison, R.E., Ilyin, a. V., Jehl, C., Rohrlich, V., Sadaqah, R.M.Y.,
883 Schidlowski, M., Sheldon, R.E., Seigmund, H., 1994. Phosphorus and phosphorites:
884 sedimentology and environments of formation. Eclogae Geol. Helv. 87, 747–788.
885 https://doi.org/10.5169/seals-167476

886 Goldhammer, T., Brüchert, V., Ferdelman, T.G., Zabel, M., 2010. Microbial sequestration of
887 phosphorus in anoxic upwelling sediments. Nat. Geosci. 3, 557–561.
888 https://doi.org/10.1038/ngeo913

889 Goldhammer, T., Brunner, B., Bernasconi, S.M., Ferdelman, T.G., Zabel, M., 2011.
890 Phosphate oxygen isotopes: Insights into sedimentary phosphorus cycling from the
891 Benguela upwelling system. Geochim. Cosmochim. Acta 75, 3741–3756.
892 https://doi.org/10.1016/j.gca.2011.04.006

893 Gunnars, A., Blomqvist, S., Martinsson, C., 2004. Inorganic formation of apatite in brackish
894 seawater from the Baltic Sea: An experimental approach. Mar. Chem. 91, 15–26.
895 https://doi.org/10.1016/j.marchem.2004.01.008

896 Haley, B.A., Klinkhammer, G.P., McManus, J., 2004. Rare earth elements in pore waters of
897 marine sediments. Geochim. Cosmochim. Acta 68, 1265–1279.
898 https://doi.org/10.1016/j.gca.2003.09.012

899 Heggie, D.T., Skyring, G.W., O'Brien, G.W., Reimers, C., Herczeg, A., Moriarty, D.J.W.,
900 Burnett, W.C., Milnes, A.R., 1990. Organic carbon cycling and modern phosphorite
901 formation on the East Australian continental margin: An overview. Geol. Soc. Spec.
902 Publ. 52, 87–117. https://doi.org/10.1144/GSL.SP.1990.052.01.07

903 Helz, G.R., Vorlicek, T.P., 2019. Precipitation of molybdenum from euxinic waters and the
904 role of organic matter. Chem. Geol. 509, 178–193.
905 https://doi.org/10.1016/j.chemgeo.2019.02.001

906 Hoetzel, S., Dupont, L.M., Marret, F., Jung, G., Wefer, G., 2017. Steps in the intensification
907 of Benguela upwelling over the Walvis Ridge during Miocene and Pliocene. Int. J. Earth
908 Sci. 106, 171–183. https://doi.org/10.1007/s00531-016-1309-0

909 Holland, H.D., 2006. The oxygenation of the atmosphere and oceans. Philos. Trans. R. Soc. B

910 Biol. Sci. 361, 903–915. https://doi.org/10.1098/rstb.2006.1838

911 Holmes, M.E., Müller, P.J., Schneider, R.R., Segl, M., Pätzold, J., Wefer, G., 1996. Stable
912 nitrogen isotopes in Angola Basin surface sediments. Mar. Geol. 134, 1–12.
913 https://doi.org/10.1016/0025-3227(96)00031-X

914 Holmkvist, L., Arning, E.T., Küster-Heins, K., Vandieken, V., Peckmann, J., Zabel, M.,
915 Jørgensen, B.B., 2010. Phosphate geochemistry, mineralization processes, and
916 Thioploca distribution in shelf sediments off central Chile. Mar. Geol. 277, 61–72.
917 https://doi.org/10.1016/j.margeo.2010.08.011

918 Ingall, E., Jahnke, R., 1994. Evidence for enhanced phosphorus regeneration from marine
919 sediments overlain by oxygen depleted waters. Geochim. Cosmochim. Acta 58, 2571–
920 2575. https://doi.org/10.1016/0016-7037(94)90033-7

921 Inthorn, M., Mohrholz, V., Zabel, M., 2006. Nepheloid layer distribution in the Benguela
922 upwelling area offshore Namibia. Deep. Res. Part I Oceanogr. Res. Pap. 53, 1423–1438.
923 https://doi.org/10.1016/j.dsr.2006.06.004

924 Jahnke, R.A., 1984. The synthesis and solubility of carbonate fluorapatite. Am. J. Sci. 284,
925 58–78. https://doi.org/10.2475/ajs.284.1.58

926 Jahnke, R.A., Emerson, S.R., Roe, K.K., Burnett, W.C., 1983. The present day formation of
927 apatite in Mexican continental margin sediments. Geochim. Cosmochim. Acta 47, 259–
928 266. https://doi.org/10.1016/0016-7037(83)90138-2

929 Jarvis, I., Burnett, W., Nathan, Y., Almbaydin, F., Attia, A.K.M., Castro, L., Flicoteaux, R.,
930 Hilmy, M., Yn, sain V.Q.A.S.A.Z., 1994. Phosphorite geochemistry state-of-the-art and
931 environmental concerns.

932 John, C.M., Föllmi, K.B., De Kaenel, E., Adatte, T., Steinmann, P., Badertscher, C., 2002.
933 Carbonaceous and Phosphate-Rich Sediments of the Miocene Monterey Formation at El
934 Capitan State Beach, California, U.S.A. J. Sediment. Res. 72, 252–267.
935 https://doi.org/10.1306/080701720252

936 Joosu, L., Lepland, A., Kirsimäe, K., Romashkin, A.E., Roberts, N.M.W., Martin, A.P., Črne,
937 A.E., 2015. The REE-composition and petrography of apatite in 2Ga Zaonega
938 Formation, Russia: The environmental setting for phosphogenesis. Chem. Geol. 395,
939 88–107. https://doi.org/10.1016/j.chemgeo.2014.11.013

Joosu, L., Lepland, A., Kreitsmann, T., Üpraus, K., Roberts, N.M.W., Paiste, P., Martin, A.P., Kirsimäe, K., 2016. Petrography and the REE-composition of apatite in the Paleoproterozoic Pilgujärvi Sedimentary Formation, Pechenga Greenstone Belt, Russia. Geochim. Cosmochim. Acta 186, 135–153. https://doi.org/10.1016/j.gca.2016.04.043

Jorgensen, B.B., 1979. A theoretical model of the stable sulfur isotope distribution in marine sediments. Geochim. Cosmochim. Acta 43, 363–374. https://doi.org/10.1016/0016-7037(79)90201-1

Krajewski, K.P., 1994. Biological processes and apatite formation in sedimentary environments. Ecol. Geol. Helvet. 87, 701–745.

Küster-Heins, K., Steinmetz, E., De Lange, G.J., Zabel, M., 2010. Phosphorus cycling in marine sediments from the continental margin off Namibia. Mar. Geol. 274, 95–106. https://doi.org/10.1016/j.margeo.2010.03.008

Lavik, G., Stührmann, T., Brüchert, V., Van Der Plas, A., Mohrholz, V., Lam, P., Mußmann, M., Fuchs, B.M., Amann, R., Lass, U., Kuypers, M.M.M., 2009. Detoxification of sulphidic African shelf waters by blooming chemolithotrophs. Nature 457, 581–584. https://doi.org/10.1038/nature07588

Lepland, A., Joosu, L., Kirsimäe, K., Prave, A.R., Romashkin, A.E., Črne, A.E., Martin, A.P., Fallick, A.E., Somelar, P., Üpraus, K., Mänd, K., Roberts, N.M.W., Van Zuilen, M.A., Wirth, R., Schreiber, A., 2014. Potential influence of sulphur bacteria on Palaeoproterozoic phosphogenesis. Nat. Geosci. 7, 20–24. https://doi.org/10.1038/ngeo2005

Lin, Z., Sun, X., Peckmann, J., Lu, Y., Xu, L., Strauss, H., Zhou, H., Gong, J., Lu, H., Teichert, B.M.A., 2016. How sulfate-driven anaerobic oxidation of methane affects the sulfur isotopic composition of pyrite: A SIMS study from the South China Sea. Chem. Geol. 440, 26–41. https://doi.org/10.1016/j.chemgeo.2016.07.007

Liu, J., Algeo, T.J., 2020. Beyond redox: Control of trace-metal enrichment in anoxic marine facies by watermass chemistry and sedimentation rate. Geochim. Cosmochim. Acta 287, 296–317. https://doi.org/10.1016/j.gca.2020.02.037

Lumiste, K., Mänd, K., Kirsimäe, K., Bailey, J., Paiste, P., Lang, L., Lepland, A., 2019. REE + Y uptake and diagenesis in Recent sedimentary apatites. Chem. Geol. 525, 268–281.

970 https://doi.org/10.1016/j.chemgeo.2019.07.034

971 Mänd, K., Kirsimäe, K., Lepland, A., Crosby, C.H., Bailey, J. V., Konhauser, K.O., Wirth,
972 R., Schreiber, A., Lumiste, K., 2018. Authigenesis of biomorphic apatite particles from
973 Benguela upwelling zone sediments off Namibia: The role of organic matter in
974 sedimentary apatite nucleation and growth. Geobiology 1–19.
975 https://doi.org/10.1111/gbi.12309

976 McArthur, J.M., 1985. Francolite geochemistry—compositional controls during formation,
977 diagenesis, metamorphism and weathering. Geochim. Cosmochim. Acta 49, 23–35.
978 https://doi.org/10.1016/0016-7037(85)90188-7

979 Meisel, S., Emeis, K.C., Struck, U., Kristen, I., 2011a. Nutrient regime and upwelling in the
980 northern Benguela since the middle Holocene in a global context - A multi-proxy
981 approach. Foss. Rec. 14, 171–193. https://doi.org/10.1002/mmng.201100006

982 Meisel, S., Struck, U., Emeis, K.C., 2011b. Nutrient dynamics and oceanographic features in
983 the central Namibian upwelling region as reflected in δ 15n-signals of suspended matter
984 and surface sediments. Foss. Rec. 14, 153–169.
985 https://doi.org/10.1002/mmng.201100005

986 Miklasz, K.A., Denny, M.W., 2010. Diatom sinking speeds: Improved predictions and insight
987 from a modified Stoke's law. Limnol. Oceanogr. 55, 2513–2525.
988 https://doi.org/10.4319/lo.2010.55.6.2513

989 Mollenhauer, G., Inthorn, M., Vogt, T., Zabel, M., Sinninghe Damsté, J.S., Eglinton, T.I.,
990 2007. Aging of marine organic matter during cross-shelf lateral transport in the
991 Benguela upwelling system revealed by compound-specific radiocarbon dating.
992 Geochemistry, Geophys. Geosystems 8. https://doi.org/10.1029/2007GC001603

993 Morford, J.L., Emerson, S.R., Breckel, E.J., Kim, S.H., 2005. Diagenesis of oxyanions (V, U,
994 Re, and Mo) in pore waters and sediments from a continental margin. Geochim.
995 Cosmochim. Acta 69, 5021–5032. https://doi.org/10.1016/j.gca.2005.05.015

996 Noffke, A., Hensen, C., Sommer, S., Scholz, F., Bohlen, L., Mosch, T., Graco, M.,
997 Wallmann, K., 2012. Benthic iron and phosphorus fluxes across the Peruvian oxygen
998 minimum zone. Limnol. Oceanogr. 57, 851–867.
999 https://doi.org/10.4319/lo.2012.57.3.0851

1000 O'Brien, G.W., Veeh, H.H., 1980. Holocene phosphorite on the East Australian continental
1001 margin. Nature 288, 690–692. https://doi.org/10.1038/288690a0

1002 Osborne, A.H., Hathorne, E.C., Schijf, J., Plancherel, Y., Böning, P., Frank, M., 2017. The
1003 potential of sedimentary foraminiferal rare earth element patterns to trace water masses
1004 in the past. Geochemistry, Geophys. Geosystems 18, 1550–1568.
1005 https://doi.org/10.1002/2016GC006782

1006 Pan, Y., Fleet, M.E., 2002. Compositions of the Apatite-Group Minerals: Substitution
1007 Mechanisms and Controlling Factors. Rev. Mineral. Geochemistry 48, 13–49.
1008 https://doi.org/10.2138/rmg.2002.48.2

1009 Paytan, A., Kastner, M., Campbell, D., Thiemens, M.H., 1998. Sulfur isotopic composition of
1010 Cenozoic seawater sulfate. Science (80-.). 282, 1459–1462.
1011 https://doi.org/10.1126/science.282.5393.1459

1012 Pedersen, T.F., Price, N.B., 1982. The geochemistry of manganese carbonate in Panama
1013 Basin sediments. Geochim. Cosmochim. Acta 46, 59–68. https://doi.org/10.1016/0016-
1014 7037(82)90290-3

1015 Peketi, A., Mazumdar, A., Joshi, R.K., Patil, D.J., Srinivas, P.L., Dayal, A.M., 2012. Tracing
1016 the Paleo sulfate-methane transition zones and H2S seepage events in marine sediments:
1017 An application of C-S-Mo systematics. Geochemistry, Geophys. Geosystems 13, 1–11.
1018 https://doi.org/10.1029/2012GC004288

1019 Pellerin, A., Antler, G., Røy, H., Findlay, A., Beulig, F., Scholze, C., Turchyn, A. V.,
1020 Jørgensen, B.B., 2018. The sulfur cycle below the sulfate-methane transition of marine
1021 sediments. Geochim. Cosmochim. Acta 239, 74–89.
1022 https://doi.org/10.1016/j.gca.2018.07.027

1023 Pichevin, L., Bertrand, P., Boussafir, M., Disnar, J.R., 2004. Organic matter accumulation
1024 and preservation controls in a deep sea modern environment: An example from
1025 Namibian slope sediments. Org. Geochem. 35, 543–559.
1026 https://doi.org/10.1016/j.orggeochem.2004.01.018

1027 Price, F.T., Shieh, Y.N., 1979. Fractionation of sulfur isotopes during laboratory synthesis of
1028 pyrite at low temperatures. Chem. Geol. 27, 245–253. https://doi.org/10.1016/0009-
1029 2541(79)90042-1

1030 Pufahl, P.K., Grimm, K.A., 2003. Coated phosphate grains: Proxy for physical, chemical, and
1031 ecological changes in seawater. Geology 31, 801–804. https://doi.org/10.1130/G19658.1

1032 Pufahl, P.K., Groat, L.A., 2017. Sedimentary and igneous phosphate deposits: Formation and
1033 exploration: An invited paper. Econ. Geol. 112, 483–516.
1034 https://doi.org/10.2113/econgeo.112.3.483

1035 Ross, J., Gao, L., Meouch, O., Anthony, E., Sutarwala, D., Mamo, H., Omelon, S., 2017.
1036 Carbonate apatite precipitation from synthetic municipal wastewater. Minerals 7.
1037 https://doi.org/10.3390/min7080129

1038 Ruttenberg, K.C., Berner, R.A., 1993. Authigenic apatite formation and burial in sediments
1039 from non-upwelling, continental margin environments. Geochim. Cosmochim. Acta 57,
1040 991–1007. https://doi.org/10.1016/0016-7037(93)90035-U

1041 Schenau, S.J., Slomp, C.P., De Lange, G.J., 2000. Phosphogenesis and active phosphorite
1042 formation in sediments from the Arabian Sea oxygen minimum zone. Mar. Geol. 169,
1043 1–20. https://doi.org/10.1016/S0025-3227(00)00083-9

1044 Schöllhorn, I., Houben, A., Gertsch, B., Adatte, T., Alexey, U., de Kaenel, E., Spangenberg,
1045 J.E., Janssen, N., Schwennicke, T., Föllmi, K.B., 2020. Enhanced upwelling and
1046 phosphorite formation in the northeastern Pacific during the late Oligocene:
1047 Depositional mechanisms, environmental conditions, and the impact of glacio-eustacy.
1048 GSA Bull. 132, 687–709. https://doi.org/10.1130/B32061.1

1049 Schuffert, J.D., Kastner, M., Jahnke, R.A., 1998. Carbon and phosphorus burial associated
1050 with modern phosphorite formation. Mar. Geol. 146, 21–31.
1051 https://doi.org/https://doi.org/10.1016/S0025-3227(97)00122-9

1052 Schulz, H., Brinkhoff, T., Ferdelman, T., Hernandez Marine, M., Teske, A., Jorgensen, B.B.,
1053 1999. Dense Populations of a Giant Sulfur Bacterium in Namibian Shelf Sediments.
1054 Science (80-.). 284, 493–495. https://doi.org/10.1126/science.284.5413.493

1055 Schulz, H., Schulz, H.N., 2005. Large Sulfur Bacteria and the Formation of Phosphorite.
1056 Science (80-.). 307, 416–418. https://doi.org/10.1126/science.1103096

1057 Shields, G.A., Stille, P., Brasier, M.D., 2000. Isotopic Records Across Two Phosphorite
1058 Giant Episodes Compared: the Precambrian-Cambrian and the Late Cretaceous-Recent.
1059 Mar. Authigenes. From Glob. to Microb. 103–115.

https://doi.org/10.2110/pec.00.66.0103

Sigman, D.M., Altabet, M.A., McCorkle, D.C., Francois, R., Fischer, G., 2000. The δ15N of nitrate in the Southern Ocean: Nitrogen cycling and circulation in the ocean interior. J. Geophys. Res. Ocean. 105, 19599–19614. https://doi.org/10.1029/2000jc000265

Sim, M.S., Bosak, T., Ono, S., 2011. Large Sulfur Isotope Fractionation Does Not Require Disproportionation. Science (80-.). 333, 74–77. https://doi.org/10.1126/science.1205103

Soares, G.G., Van Kranendonk, M.J., Belousova, E., Thomson, S., 2019. Phosphogenesis in the immediate aftermath of the Great Oxidation Event: Evidence from the Turee Creek Group, Western Australia. Precambrian Res. 320, 193–212. https://doi.org/10.1016/j.precamres.2018.10.017

Theiling, B.P., Coleman, M., 2019. The relationship of diagenesis with a complex microbial ecosystem in the phosphatic interval of the Miocene Monterey Formation: evidence from stable isotopes and mineralogy. Mar. Geol. 413, 112–128. https://doi.org/10.1016/j.margeo.2019.04.001

Tribovillard, N., Algeo, T.J., Baudin, F., Riboulleau, A., 2012. Analysis of marine environmental conditions based on molybdenum-uranium covariation-Applications to Mesozoic paleoceanography. Chem. Geol. 324–325, 46–58. https://doi.org/10.1016/j.chemgeo.2011.09.009

Tribovillard, N., Algeo, T.J., Lyons, T., Riboulleau, A., 2006. Trace metals as paleoredox and paleoproductivity proxies: An update. Chem. Geol. 232, 12–32. https://doi.org/10.1016/j.chemgeo.2006.02.012

Tyrrell T., 1999. The relative influences of nitrogen and phosphorus on oceanic primary production. Nature 400, 525–531.

Tyrrell, T., Lucas, M.I., 2002. Geochemical evidence of denitrification in the Benguela upwelling system. Cont. Shelf Res. 22, 2497–2511. https://doi.org/10.1016/S0278-4343(02)00077-8

Wallin, B., 1989. Origin of the Lower Cambrian phosphatic bed at Vassbo, Sweden. Terra Nov. 1, 274–279. https://doi.org/10.1111/j.1365-3121.1989.tb00369.x

Wanty, R.B., Goldhaber, M.B., 1992. Thermodynamics and kinetics of reactions involving

vanadium in natural systems: Accumulation of vanadium in sedimentary rocks. Geochim. Cosmochim. Acta 56, 1471–1483. https://doi.org/10.1016/0016-7037(92)90217-7

Wu, F., Owens, J.D., Tang, L., Dong, Y., Huang, F., 2019. Vanadium isotopic fractionation during the formation of marine ferromanganese crusts and nodules. Geochim. Cosmochim. Acta. https://doi.org/10.1016/j.gca.2019.09.007

Zhang, C.L., Huang, Z., Cantu, J., Pancost, R.D., Brigmon, R.L., Lyons, T.W., Sassen, R., 2005. Lipid biomarkers and carbon isotope signatures of a microbial (Beggiatoa) mat associated with gas hydrates in the Gulf of Mexico. Appl. Environ. Microbiol. 71, 2106–2112. https://doi.org/10.1128/AEM.71.4.2106-2112.2005

Zoss, R., Medina Ferrer, F., Flood, B.E., Jones, D.S., Louw, D.C., Bailey, J., 2018. Microbial communities associated with phosphogenic sediments and phosphoclast-associated DNA of the Benguela upwelling system. Geobiology 17, 76–90. https://doi.org/10.1111/gbi.12318

Figures

Figure 1. Geological map of the Namibian Shelf showing the coring site. Modified after Brüchert et al. (2006).

Figure 2. Scanning electron microscope images of: (a-b) bulk sediments, (c-d) apatite grains with non-phosphatic film coatings and (e-f) apatite grain morphology showing irregular and pitted surfaces- Figures a-d are backscattered electron images, e-f are secondary electron images. Ap. – apatite grains, Dia. –diatom frustules.

Figure 3. Phosphorus and sulfur content in Core 25005 (wt.%). Data for P and S from Mänd et al. (2018).

Figure 4. Depth profile of redox-sensitive element concentrations and proxy values: (a) Mo/Al (b) V/Al, (c) U/Al ratios, (d) Re/Al ratios. Dashed lines mark the transition from phosphatic to non-phosphatic sediments.

Figure 5. Depth profiles of (a) $\delta^{13}C_{org}$ (b) total organic carbon, (c) $\delta^{15}N$.

Figure 6. $\delta^{34}S$ composition of different sulfur phases: (a) chromium reducible sulfur, (b) phosphate associated sulfate (PAS) and easily extractable sulfate (EES). Modern seawater sulfate value from Paytan et al. (1998).

Figure 7. Total organic carbon and trace metal covariation: (a) molybdenum – TOC covariation plot. Modified after Algeo and Tribovillard (2009), (b) uranium – TOC covariation.

Figure 8. Depth profile of Mn/Al. Dashed lines mark the transition from phosphatic to non-phosphatic sediments.

Figure 9. Corg/P ratios of Core 25005. Dashed lines mark the transition from phosphatic to non-phosphatic sediments.

Figure 10. Mixing model of PAS $\delta^{34}S$ values. Mixing line endmembers used were the lightest CRS value measured from the samples (-22.14‰) and modern seawater sulfate value (21‰; Paytan et al., 1998).

Figure 11. Correlation between TOC (%) and $\delta^{13}C_{org}$ (‰).

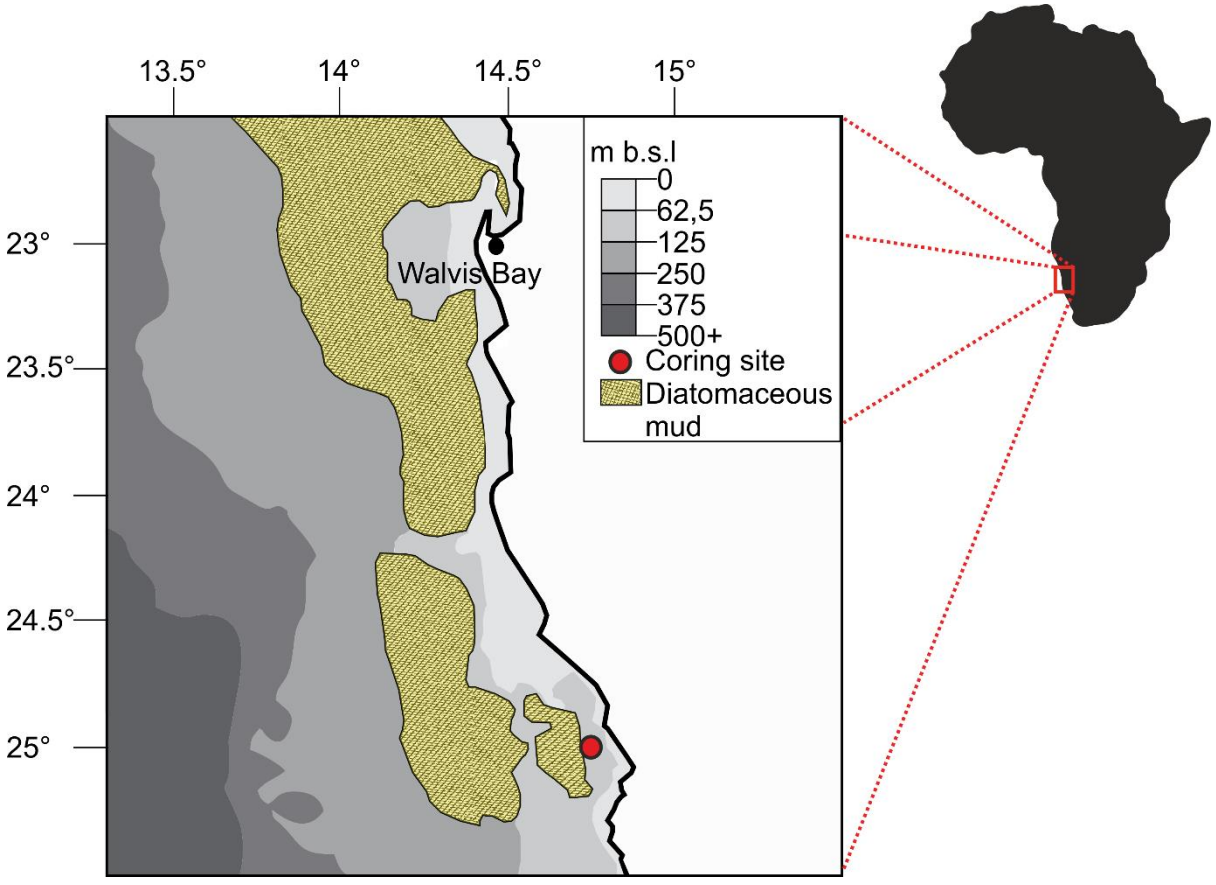

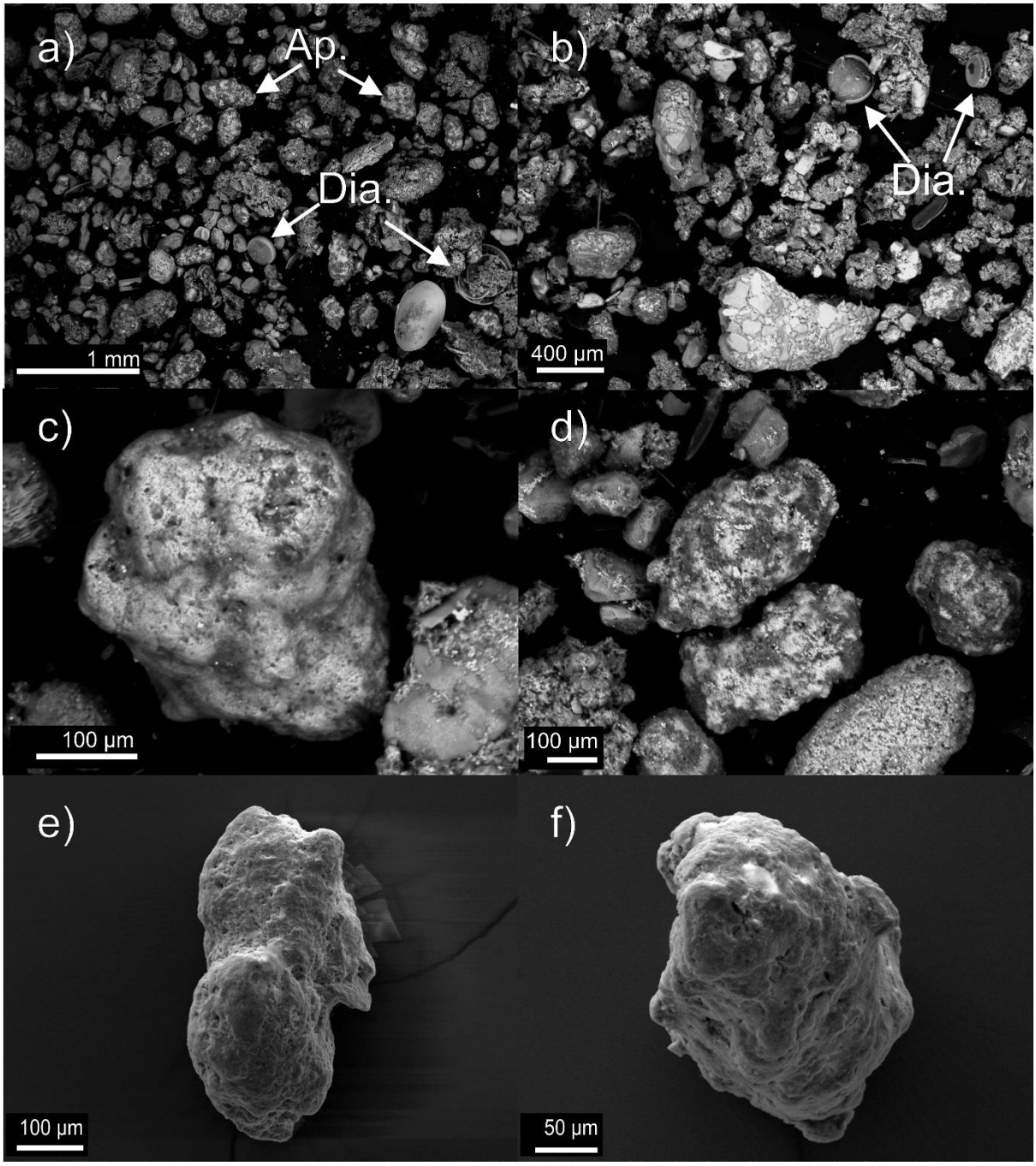

1131

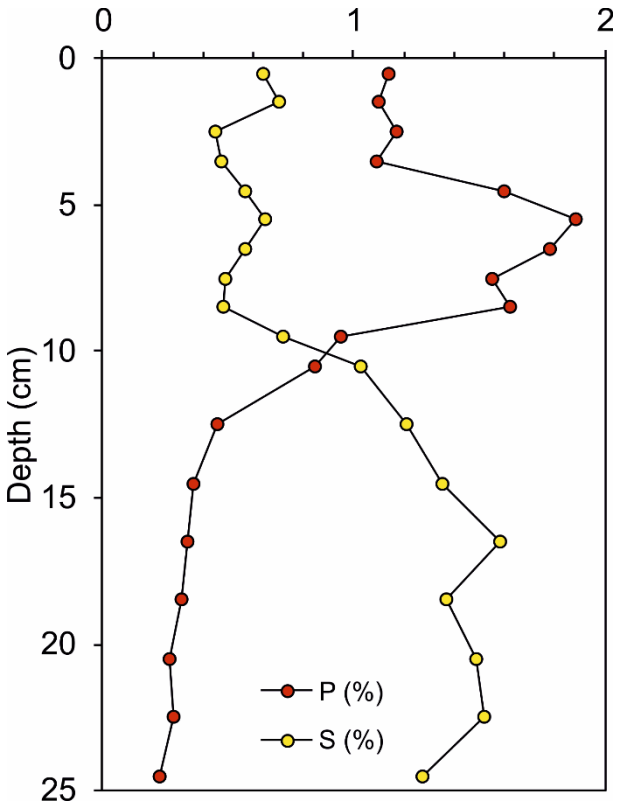
0
1
2
0
5
10
15
20
25
Depth (cm)
P (%)
S (%)

1132

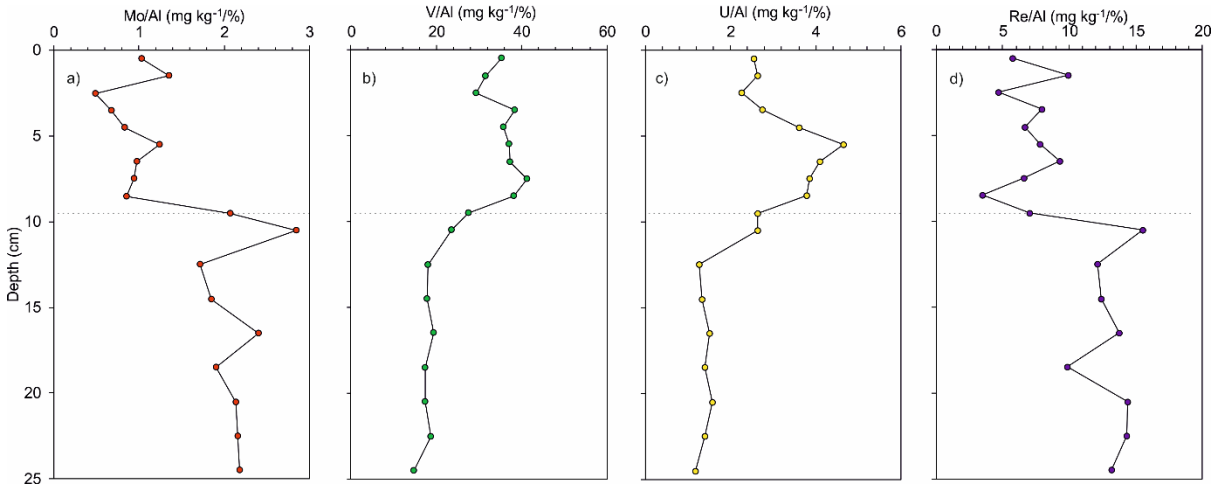
Mo/Al (mg kg-1/%)
V/Al (mg kg-1/%)
U/Al (mg kg-1/%)
Re/Al (mg kg-1/%)
a)
b)
c)
d)
Depth (cm)

1133

1134

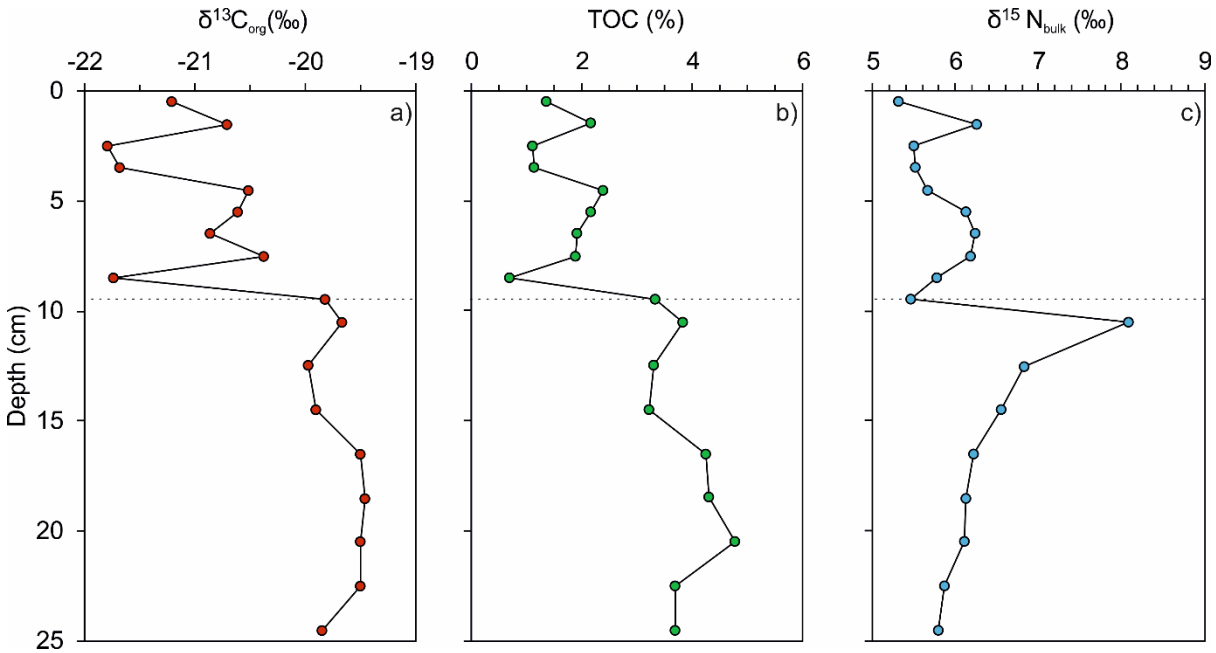
δ13Corg(‰)
-22
-21
-20
-19
TOC (%)
0
2
4
6
δ15 Nbulk (‰)
5
6
7
8
9
Depth (cm)
0
5
10
15
20
25
a)
b)
c)

1135

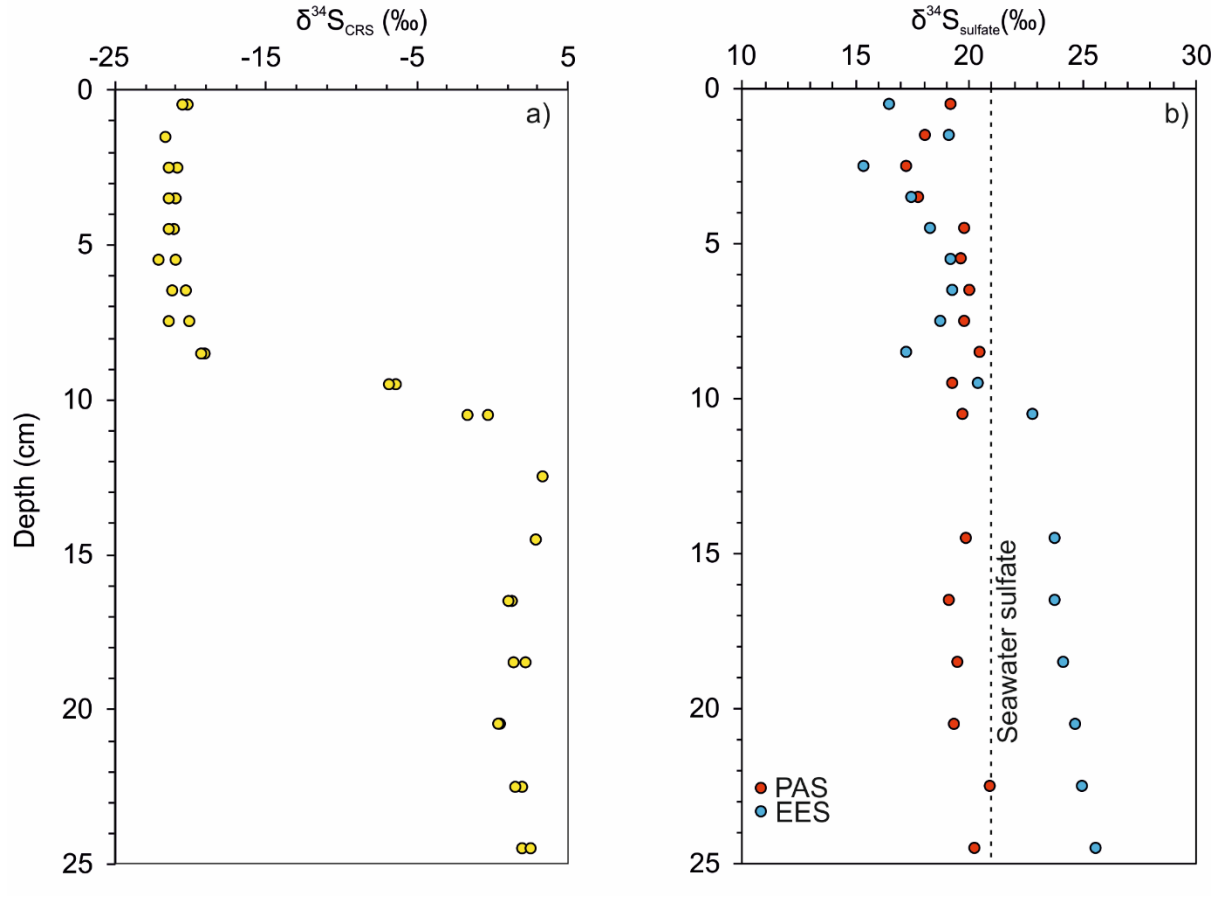
δ34SCRS (‰)
-25
-15
-5
5
δ34Ssulfate(‰)
10
15
20
25
30
Depth (cm)
0
5
10
15
20
25
a)
b)
Seawater sulfate
PAS
EES

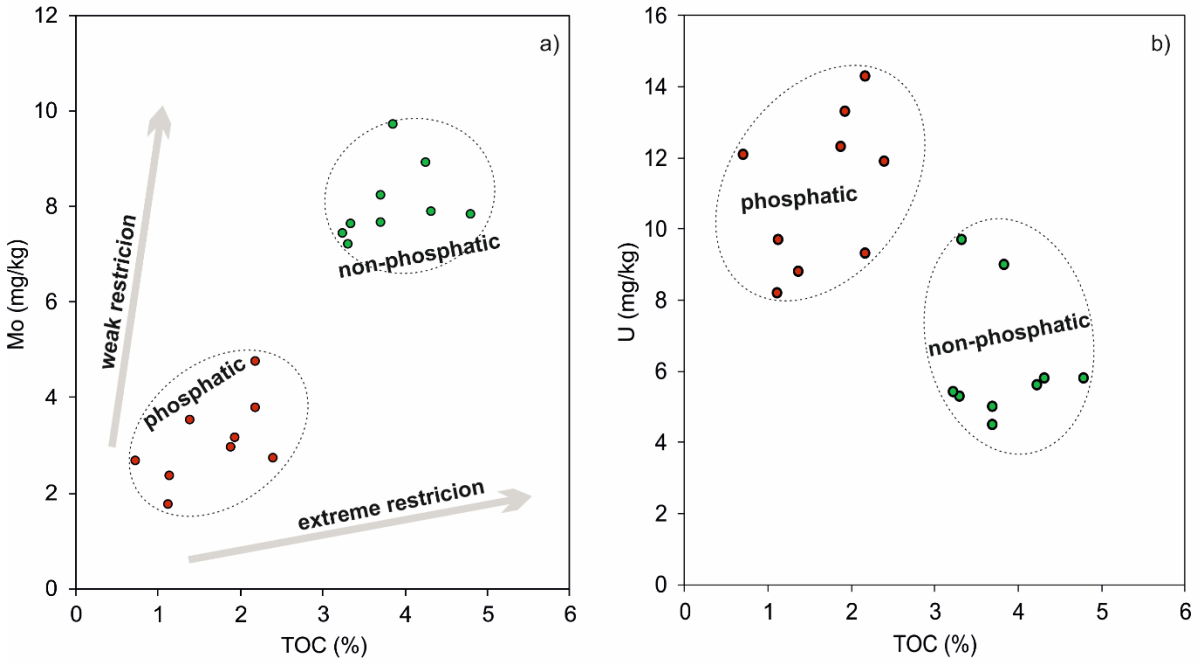
a)
Mo (mg/kg)
TOC (%)
weak restricion
extreme restricion
phosphatic
non-phosphatic
b)
U (mg/kg)
TOC (%)
phosphatic
non-phosphatic

1136

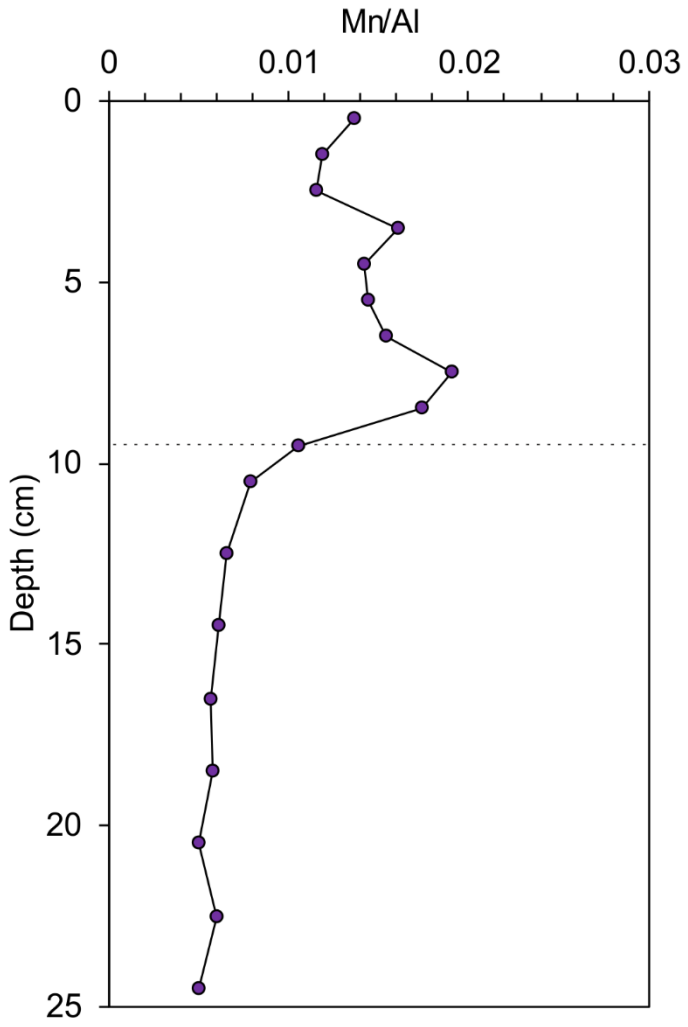
Mn/Al
Depth (cm)

1137

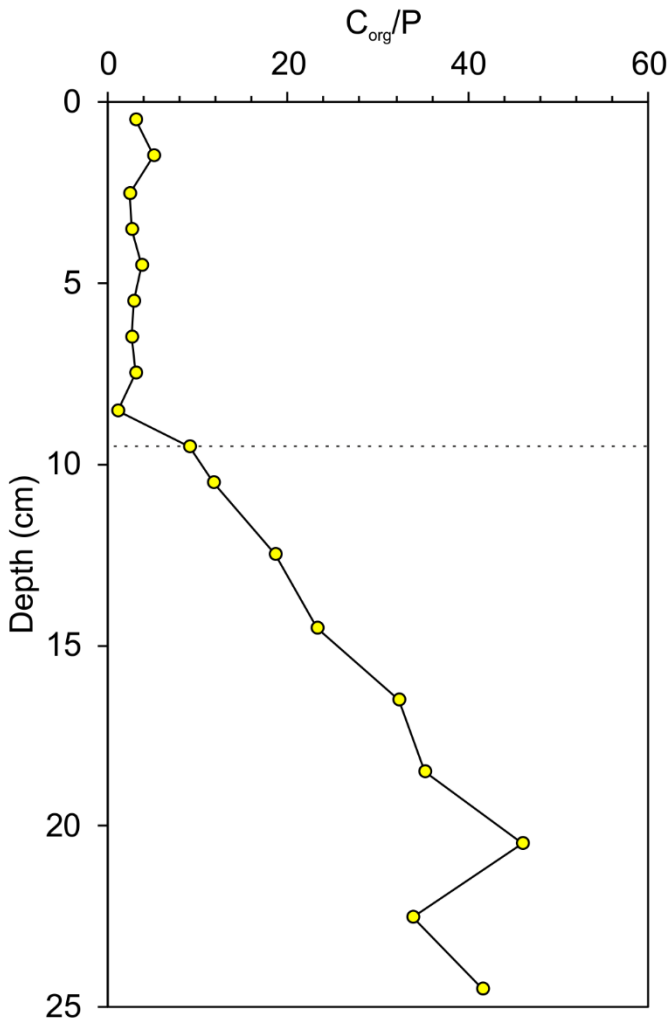

1138

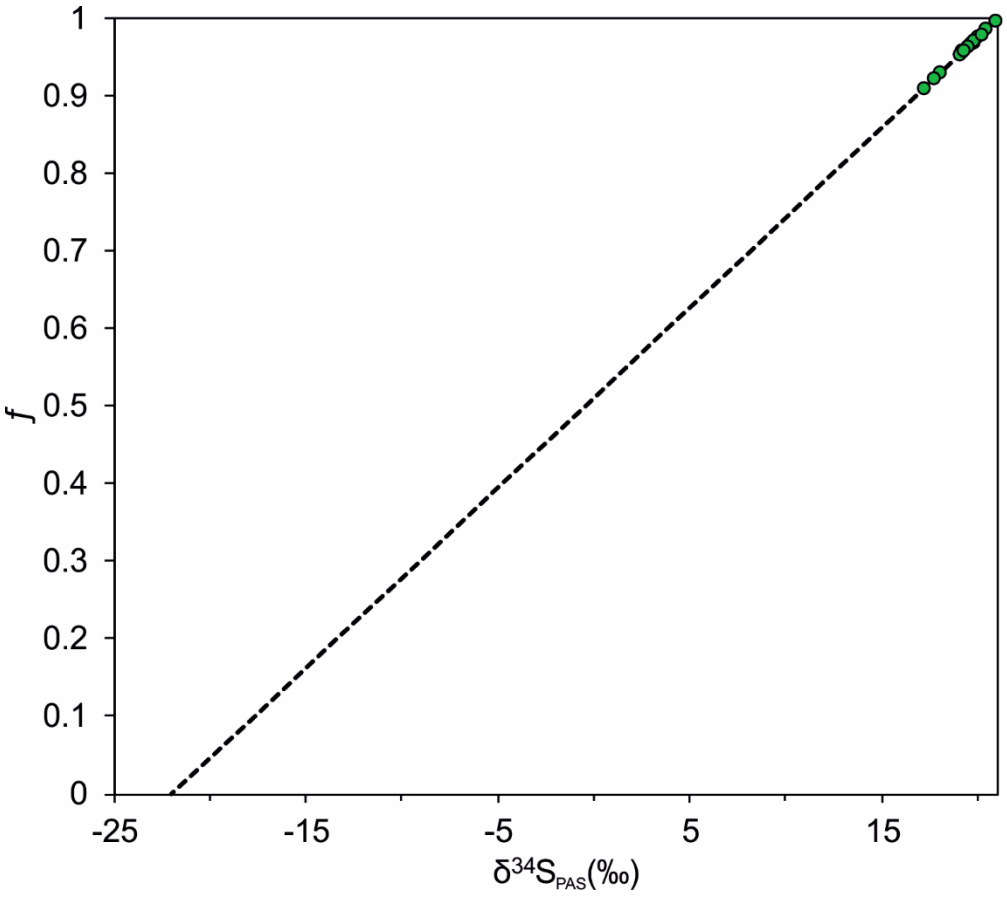
1
0.9
0.8
0.7
0.6
0.5
0.4
0.3
0.2
0.1
0
f
-25
-15
-5
5
15
δ34SPAS(‰)

1139

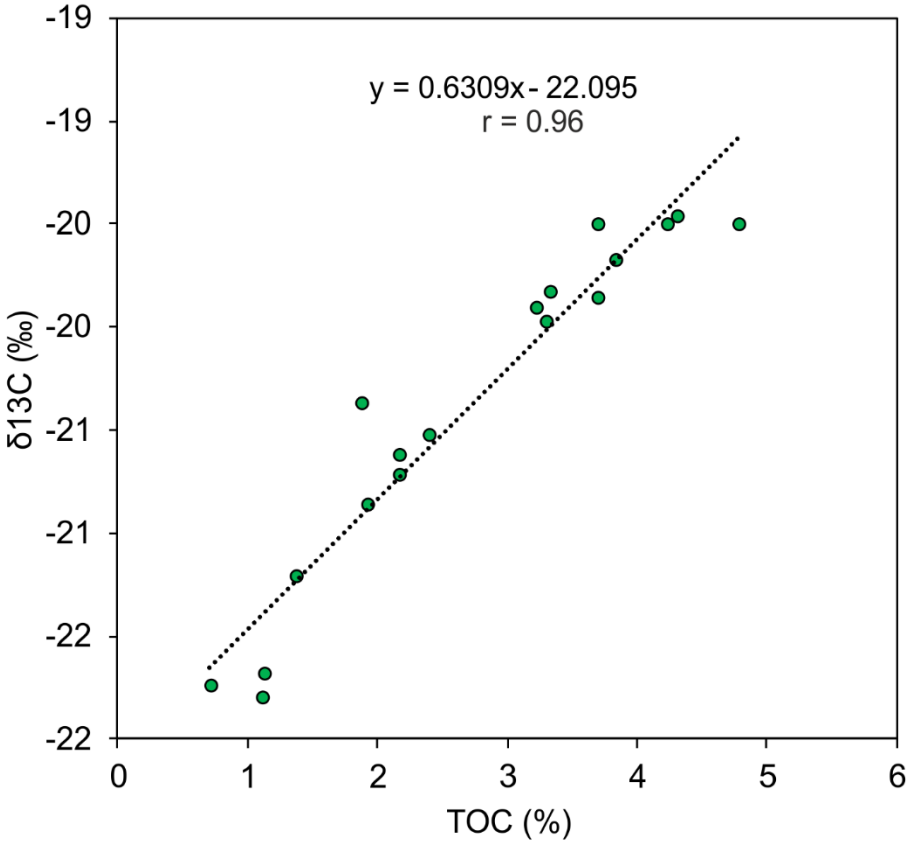
y = 0.6309x - 22.095
r = 0.96
-19
-19
-20
-20
-21
-21
-22
-22
δ13C (‰)
0
1
2
3
4
5
6
TOC (%)

1140